Darwinian properties and their trade-offs in autocatalytic RNA networks

Sandeep Ameta[1,‡], Simon Arsène[1,‡], Sophie Foulon[1], Baptiste Saudemont[1], Bryce E. Clifton[2], Andrew D. Griffiths[1,], Philippe Nghe[1,*]*

Affiliations

[1]Laboratoire de Biochimie, CNRS UMR8231, Chimie Biologie Innovation, ESPCI Paris, 10 Rue Vauquelin, 75005, Paris, France

[2]School of Chemistry and Biochemistry, Georgia Institute of Technology, Atlanta, Georgia 30332-0400

[‡]Sandeep Ameta and Simon Arsène contributed equally to the work.

Correspondence to: andrew.griffiths@espci.fr, philippe.nghe@espci.fr

Abstract

Evolution *via* template-based replication[1-4] was probably preceded by a more rudimentary form of evolution based on networks of autocatalytic reactions[5-8]. However, reaction networks possessing the Darwinian properties of variation (in composition, the catalysts present and their relative amounts), differential reproduction (accumulation of products), and heredity (persistence of composition), have so far not been identified. Here we show that networks of catalytic RNAs can possess certain properties of Darwinian systems, that these properties are controlled by network topology, and characterize important trade-offs between them. By combining barcoded sequencing with droplet microfluidics, we screened ~20,000 reactions corresponding to more than 1,800 distinct networks of ribozymes that catalyse their own formation from RNA fragments. We found that more highly connected networks tend to reproduce more quickly (accumulate more ribozymes) and be more robust to perturbations, indicating a trade-off between variation and reproduction. Variations are strongest when adding upstream ribozymes with novel reaction specificities (innovations) which target weakly connected networks. In turn, innovations increase connectivity, thus buffer against further perturbations, highlighting a second trade-off between robustness and variation. Despite this, phases of compositional robustness can alternate with sudden variations of the composition across trajectories of network growth by accretion of novel species. Finally, heredity is found to be limited by the activity of self-assembled, non-covalent ribozymes. Our findings show that connectivity in reaction networks not only determines the probability of autocatalytic sets in chemistries[8], but also their potential for evolution. They are directly relevant to scenarios where early evolution is driven by environmental heterogeneity[9,10], as it depends both on robustness (persistence being necessary for selection to act) and susceptibility to changes (in order to explore novel states). More broadly, they provide guiding rules for chemistries capable of Darwinian evolution and constrain scenarios of the origins of life.

Main

In the prebiotic world, the spontaneous appearance of an RNA polymerase ribozyme (a replicase) with sufficient processivity to allow self-replication and enough fidelity to avoid an error catastrophe[5,6] seems unlikely, given that known replicases are long (>165 nt) and structurally complex[1-4]. However, theoretical studies suggest that earlier modes of evolution could have been supported by autocatalytic sets, where reproduction results from networks of more rudimentary catalysts[11-13]. Consistently, recent experiments indicate that RNA polymerase ribozymes can assemble from catalytic networks of RNA oligomers[14], suggesting that replicases may have emerged as components of such networks. Nevertheless, sustaining evolution in reaction networks is by no means trivial, as the Darwinian properties of variation, heredity and selection are mediated by chemical compositions (the proportion of different chemical species) rather than the copying of a sequence. Furthermore, the possibility to evolve chemistries may be constained by trade-offs between these properties. For instance, robustness to environmental perturbations and persistence of compositions are necessary for selection to act, but must be balanced with variation to explore novel states. So far, none of these Darwinian properties, nor their interplay, have been experimentally studied at a large scale in a prebiotically relevant system.

We studied an experimental model of autocatalytic RNAs derived from the group I intron of the *Azoarcus* bacterium[15]. Fragments (denoted WXY and Z) assemble into non-covalent complexes that catalyze the formation of more efficient covalent ribozymes[16,17] (denoted WXYZ, Fig. 1a), which in turn catalyze with higher efficiency the formation of further covalent ribozymes, allowing the formation of autocatalytic networks[16]. Three nucleotide long sequences, called internal guide (IGS) and target (tag), located at extremities of the WXY fragments[16] (Fig. 1a, top left), determine catalytic specificity by base-pairing between a ribozyme IGS and a fragment tag. Combinations of such fragments yield networks of diverse connectivity (Fig 1a, bottom center)[18]. These networks can be represented in a coarse-grained manner by directed graphs (Fig. 1a, top right): a node representing both non-covalent and covalent ribozyme species with the same IGS and tag, and a directed edge points from an upstream ribozyme species to the downstream ribozyme species whose formation it catalyses.

We developed a method to generate and measure a high diversity of such RNA reaction networks, using droplet microfluidics coupled to barcoded Next-Generation Sequencing (Fig. 1b-c, Extended Data Fig. 1). It consists of first producing a library of 5 pL droplets containing 24 different combinations of the 16 WXY fragments (Extended Data Table 1), together with

92 hairpin RNA reporters that do not react but enable later identification of the mixture of WXY
93 fragments by sequencing. The 24 initial combinations were selected among a random sample
94 by minimizing their mutual overlap while covering as evenly as possible network sizes from 1
95 to 16 species after combinatorial droplet fusion (see below and Methods). Random sets
96 comprising 1 to 5 droplets of this initial library were then electrocoalesced[19] with a 50 pL
97 droplet containing the reaction buffer and Z fragments. After incubation at 48°C for 1 hour, the
98 composition of each droplet was analyzed by droplet-level RNA sequencing adapted from
99 single-cell transcriptomics[20]. Hydrogel beads carrying cDNA primers with a barcode specific
100 to each bead (Extended Data Fig. 2) were encapsulated one-by-one in droplets then fused with
101 the RNA containing droplets, followed by primer release and cDNA synthesis (Fig. 1c,
102 Extended Data Fig. 1, and Methods). Barcoded cDNAs were recovered and sequenced. All the
103 reads from a same droplet carry the same barcode (Extended Data Fig. 3a, b).
104 The initial combinations of fragments (encoded by hairpin RNA reporters, Extended Data Fig.
105 3, 4), and the final fraction of ribozymes produced during incubation were determined in
106 20,038 droplets, comprising 1,837 unique networks with on average 11 replicates each (Fig. 1d,
107 Extended Data Fig. 5a), indicating a mean precision of ~6% in species fractions (Extended Data
108 Fig. 5b). Repeatability was tested with a full experimental replicate (r=0.84 between species
109 fractions), and droplet cross-talk was quantified to be ~13% (Extended Data Fig. 5c-e).
110 We observed highly heterogeneous patterns of covalent ribozyme accumulation, demonstrating
111 the existence of interdependences between reaction network components (Fig. 1d). Indeed, if
112 every ribozyme species were reacting independently, the relative rank between any pair of
113 ribozyme species would be conserved across all networks. On the contrary, we observed that
114 for 63% of ribozyme pairs, their relative ranking differed in at least 10% of the networks
115 (Extended Data Fig. 6a), extending previous findings of non-conserved ranking in a small set
116 of such networks[21]. This diversity in species fractions in networks was well predicted by a
117 kinetic model without fitting parameters (Methods) by adding the first order effective catalytic
118 rates of non-covalent and covalent ribozymes measured independently for individual IGS-tag
119 pairs ($r=0.83$, $p<10^{-3}$, Fig. 1 e-f, Extended Data Fig. 6 b-d).
120 Comparing networks generated from distinct substrate sets also revealed differences in growth,
121 quantified as the concentration of covalent ribozyme accumulated during the reaction relatively
122 to hairpin reporters of known concentration (Fig. 2a): yield varied 10-fold across networks
123 comprising between 2 and 15 species (see Extended Data Table 2), and up to 6-fold within
124 networks of the same size but with different topologies (Fig. 2a).

We then quantified variations in response to the addition of WXY fragments allowing the formation of a novel ribozyme. This corresponds to comparing networks G and G' differing by a single node a (networks connected by a curved line in Fig. 1d). Denoting V the set of nodes common to G and G', the total perturbation is defined as $p_{G\to G'} = \sum_{v\in V} |y'_v - y_v|$ where y_v and y'_v are the respective fractions of species v in G and G', both normalized within V (Fig. 2b). By definition, the maximum is $p_{G\to G'} = 2$ and is reached for a full switch in species composition, for example going from $(y_u, y_v) = (0, 1)$ to $(y'_u, y'_v) = (1, 0)$ in $V = \{u, v\}$.

Averaging for each network the effect of all perturbations (green line, Fig. 2c,) revealed large differences from marginally to strongly perturbable networks (mean $\bar{p}_{G\to G'}$ from 0.1 to 1). Furthermore, we observed a trade-off between growth and variation (Fig. 2d), implying that high yield networks tend to be poorly perturbable.

We aimed to interpret the diversity of observed responses based on network connectivity. The kinetic model does not provide such a direct interpretation as it consists of a mixture between two regimes, where either only non-covalent or only covalent ribozymes are active. For non-covalent ribozymes only, species fractions should be predicted by in-degree centrality, a network-theoretic measure which accounts only for catalysis by directly upstream ribozymes[22]. In contrast, for covalent ribozymes only, species fractions should be predicted by eigenvector centrality, which accounts for longer catalytic chains[22]. Despite these differences, the in-degree centrality was found to be a good approximation of the eigenvector centrality (for our dataset, R=0.83, p-value<10^{-5}, Extended Data Fig. 7a), as is already known in general[23], except for strongly selfish ribozymes which fraction is underestimated (13% of the dataset, Extended Data Fig. 7b).

The in-degree centrality approximation allowed an analytical derivation of the perturbations (Supplementary File 1),

$$p_{G\to G'} = 2n\frac{1 - n\,\dfrac{m}{\sigma_G/e}}{\sigma_G/e + n} \quad (1),$$

with 4 control parameters (Fig. 3a): n is the *perturbation breadth*, the number of targets of the new node a introduced in the network; m is the *catalytic novelty*, the number of catalysts already present in G with the same IGS as a (novelty being higher for lower m); σ_G is the *background strength*, the sum of all edge weights in the network, and; e is the catalytic strength e of edges outgoing from a as determined by its IGS.

The influence of parameters σ_G, e, m, and n on $p_{G\to G'}$ predicted by the in-degree approximation (Equation 1, continuous curves in Fig. 3b) was similar to those predicted by eigenvector

157 centrality (Fig. 3b, dots), and, more importantly, were well verified experimentally (Fig. 3b,
158 compare left and right panels). First, perturbation strength was impacted much more strongly
159 by catalytic novelty m (Fig. 3b, bottom) than by perturbation breadth n for the values tested
160 here (n = 1 or 2, Fig. 3b, top). Second, Equation (1) poses the condition $\sigma_G/e \leq n$ for
161 significant variations, consistent with high values $p_{G\to G'}$ being observed only when $\sigma_G/e < 2$
162 (given that $n \leq 2$, Fig. 3b, top). Overall, the highest perturbations $p_{G\to G'}$ required a catalytic
163 innovation ($m = 0$, i.e. a new IGS) to be combined with a low normalized background strength
164 ($\sigma_G/e \leq 1$). Perturbations were indeed up to 10 times higher in such cases, compared to cases
165 where either $m > 0$ or $\sigma_G/e > 2$ (Fig. 3b, bottom). Interestingly, the model indicated that
166 perturbations should peak at intermediate values of σ_G/e when $m > 0$ (purple line, Fig 3b, right),
167 which was consistently observed in the data but not significant (purple line, Fig 3b, left). The
168 predictions of Equation 1 were also verified for other values of the parameters (Extended Data
169 Fig. 8) and at the level of single nodes (Extended Data Fig. 9). In addition, the attenuation of
170 perturbations with large σ_G/e combined with the weak but significant correlation between
171 growth and σ_G (R=0.5, $p<10^{-5}$, Fig. 3c) explains part of the trade-off between growth and
172 perturbability reported in Fig. 2d.
173 To test the interplay between robustness and variation in scenarios where novel species would
174 appear either spontaneously[13] or due to changes in substrates provided from the prebiotic
175 milieu[9,10], we analyzed cumulative perturbations across trajectories of network growth, starting
176 from networks with three nodes, randomly adding one node at a time (Fig. 4a). We have seen
177 that strong perturbations require catalytic innovations ($m = 0$). In such case, Equation 1
178 reduces to $p_{G\to G'} = 2/(1 + \sigma_G/ne)$. The ratio σ_G/ne expresses a second trade-off, between
179 the robustness induced by the background strength of the network σ_G, and the variation induced
180 by the novel catalyst as characterized by n and e.
181 As for a large perturbation to occur, ne must be comparable to the σ_G of the perturbed network,
182 σ_G would roughly double after a strong perturbation, enhancing robustness to further variation.
183 Consequently, strong variations should be followed by small ones, and result in inflexions
184 (change in curvature) in cumulative perturbation trajectories. We quantified the corresponding
185 inflexions by their sharpness (third derivative at inflexion, Extended Data Fig. 10a), and
186 categorized them as strong when in the top 25% of sharpness (Fig. 4b). Comparing the
187 distributions of sharpness for all inflexion points showed that they are, as predicted,
188 significantly sharper for catalytic innovations (Fig. 4c). Consistently, the number of strong
189 inflexions correlates with the number of catalytic innovations per trajectory (Fig. 4d).

Although introducing a node causing a strong perturbation buffers the resulting network against further perturbations, subsequent variations along trajectories are still possible, as exemplified in Fig. 4a, b. By computationally analysing trajectories for an extended repertoire of specific interactions, we found that sustained variation requires perturbing species of increasing targeting breadth n (Fig. 4e) and increased waiting time between variation events (until the diversity of IGS/tag pairs saturates) Fig. 4f). The former allows the ever larger σ_G values to be overcome, while the latter corresponds to the build-up of weakly connected nodes that can become targets. Interestingly, the trade-off between σ_G and ne translates at the level of trajectories: chemistries with a high density of catalytic interactions lead to many trajectories with a few inflexions, while sparse chemistries lead to fewer trajectories but with many inflexions (Fig. 4g).

We have shown experimentally that a diversity network behaviour can be generated from a small set of interactions, and that these networks can possess Darwinian properties. What is missing, therefore, for such a system to evolve? First, we found that network topology imposes trade-offs between growth and variation, and between variation and robustness. In particular, the density of interactions in a chemistry should neither too sparse, nor too dense to potentially allow evolution. Second, heredity, which in the context of autocatalytic networks depends on the persistence of the chemical composition over time is weakened due to catalysis by self-assembled, non-covalent, complexes. This leads to relaxation of chemical compositions toward states determined by the substrates rather than by the covalent catalysts transmitted from pre-existing networks (Extended Data Fig. 11). Reducing catalysis by self- non-covalent complexes may sufficiently enhance heritability for the system to evolve, if combined with selection and variation. On the other hand, self-assembled catalysts could facilitate the emergence of novel catalysts from variation in the substrates provided from environment.

References

1. Horning, D. P. & Joyce, G. F. Amplification of RNA by an RNA polymerase ribozyme. *Proc. Natl. Acad. Sci. U.S.A.* **113**, 9786-9791 (2016).
2. Johnston, W. K., Unrau, P. J., Lawrence, M. S., Glasner, M. E. & Bartel, D. P. RNA-catalyzed RNA polymerization: accurate and general RNA-templated primer extension. *Science* **292**, 1319-1325 (2001).
3. Kim, D. E. & Joyce, G. F. Cross-catalytic replication of an RNA ligase ribozyme. *Chem. Biol.* **11**, 1505-1512 (2004).
4. Wochner, A., Attwater, J., Coulson, A. & Holliger, P. Ribozyme-catalyzed transcription of an active ribozyme. *Science* **332**, 209-212 (2011).
5. Eigen, M. Selforganization of matter and the evolution of biological macromolecules. *Naturwissenschaften* **58**, 465-523 (1971).
6. Eigen, M. & Schuster, P. The hypercycle. A principle of natural self-organization. Part A: Emergence of the hypercycle. *Naturwissenschaften* **64**, 541-565 (1977).
7. Hordijk, W., Steel, M. & Kauffman, S. The structure of autocatalytic sets: evolvability, enablement, and emergence. *Acta. Biotheor.* **60**, 379-392 (2012).
8. Kauffman, S. A. Autocatalytic sets of proteins. *J. Theor. Biol.* **119**, 1-24 (1986).
9. Abbott, S. S., Harrison, T. M., Schmitt, A. K. & Mojzsis, S. J. A search for thermal excursions from ancient extraterrestrial impacts using Hadean zircon Ti-U-Th-Pb depth profiles. *Proc. Natl. Acad. Sci. U.S.A.* **109**, 13486-13492 (2012).
10. Stueken, E. E. *et al.* Did life originate from a global chemical reactor? *Geobiology* **11**, 101-126 (2013).
11. Jain, S. & Krishna, S. A model for the emergence of cooperation, interdependence, and structure in evolving networks. *Proc. Natl. Acad. Sci. U.S.A.* **98**, 543-547 (2001).
12. Nghe, P. *et al.* Prebiotic network evolution: six key parameters. *Mol. Biosyst.* **11**, 3206-3217 (2015).
13. Vasas, V., Fernando, C., Santos, M., Kauffman, S. & Szathmáry, E. Evolution before genes. *Biol. Direct* **7**, 1; discussion 1 (2012).
14. Mutschler, H., Wochner, A. & Holliger, P. Freeze-thaw cycles as drivers of complex ribozyme assembly. *Nat. Chem.* **7**, 502-508 (2015).
15. Reinhold-Hurek, B. & Shub, D. A. Self-splicing introns in tRNA genes of widely divergent bacteria. *Nature* **357**, 173-176 (1992).
16. Draper, W. E., Hayden, E. J. & Lehman, N. Mechanisms of covalent self-assembly of the Azoarcus ribozyme from four fragment oligonucleotides. *Nucleic Acids Res.* **36**, 520-531 (2008).
17. Hayden, E. J., von Kiedrowski, G. & Lehman, N. Systems chemistry on ribozyme self-construction: evidence for anabolic autocatalysis in a recombination network. *Angew. Chem. Int. Ed. Engl.* **47**, 8424-8428 (2008).
18. Vaidya, N. *et al.* Spontaneous network formation among cooperative RNA replicators. *Nature* **491**, 72-77 (2012).
19. Chabert, M., Dorfman, K. D. & Viovy, J. L. Droplet fusion by alternating current (AC) field electrocoalescence in microchannels. *Electrophoresis* **26**, 3706-3715 (2005).
20. Klein, A. M. *et al.* Droplet barcoding for single-cell transcriptomics applied to embryonic stem cells. *Cell* **161**, 1187-1201 (2015).
21. Yeates, J. A., Hilbe, C., Zwick, M., Nowak, M. A. & Lehman, N. Dynamics of prebiotic RNA reproduction illuminated by chemical game theory. *Proc. Natl. Acad. Sci. U.S.A.* **113**, 5030-5035 (2016).
22. Yeates, J. A. M., Nghe, P. & Lehman, N. Topological and thermodynamic factors that influence the evolution of small networks of catalytic RNA species. *RNA* **23**, 1088-1096 (2017).
23. Valente, T. W., Coronges, K., Lakon, C. & Costenbader, E. How Correlated Are Network Centrality Measures? *Connect (Tor. Ont.)* **28**, 16-26 (2008).

24. Krzywinski, M. *et al.* Circos: an information aesthetic for comparative genomics. *Genome Res.* **19**, 1639-1645 (2009).

Figures

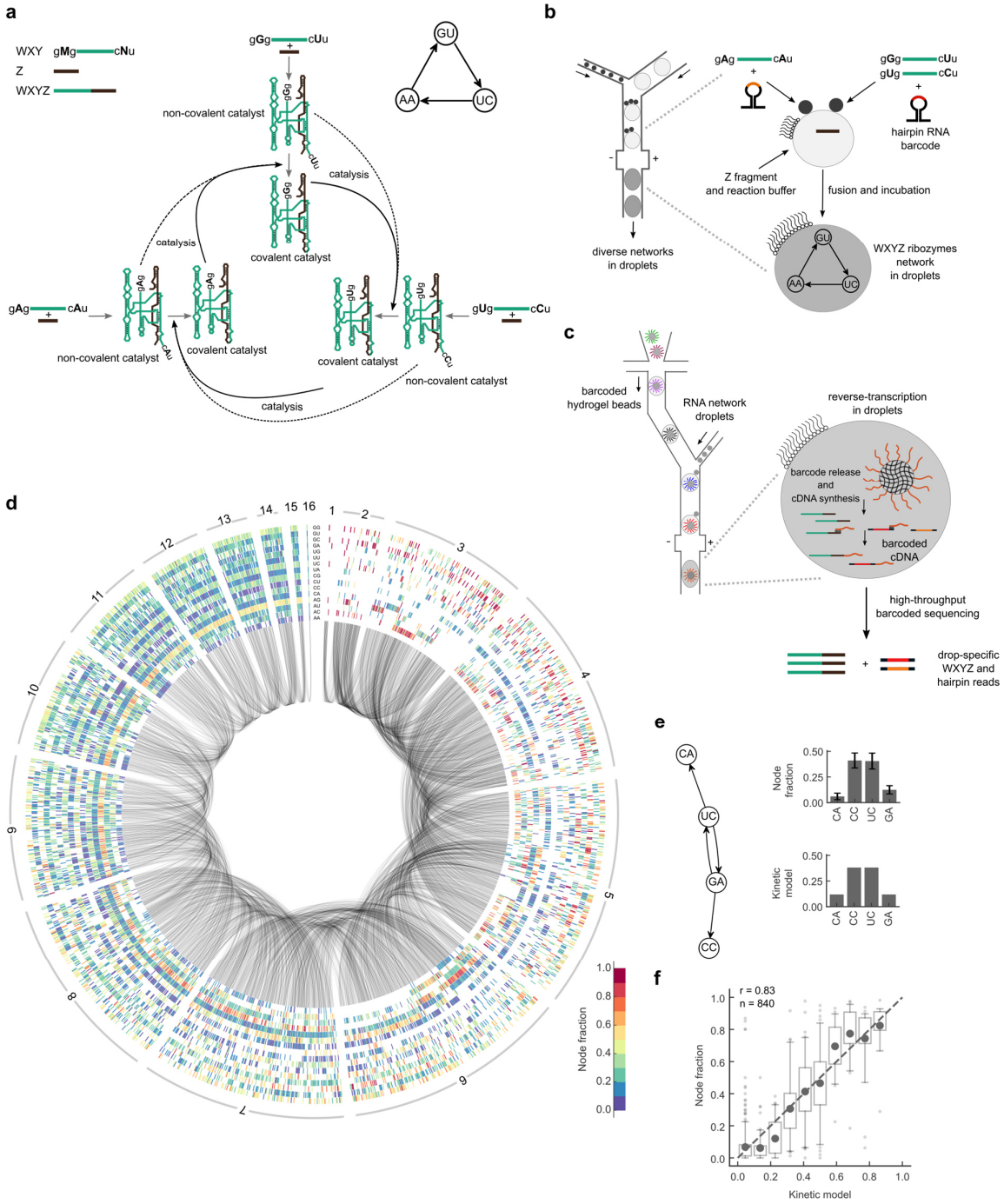

Fig. 1. Experimental set-up and RNA network compositional landscape. a, Top left: RNA fragments, named WYX and Z, can be assembled into full length ribozymes WXYZ (both non-covalent and covalent catalysts). WYX fragments each comprise 3 nucleotide long IGS and tag sequences, respectively denoted g**M**g and c**N**u, where **M**, **N** can be varied, resulting in 16 different combinations[18]. Bottom center panel: The base-pairing interactions between **M** and **N** determine the specificity of full length catalysts for their substrate fragments. In this example, each of the 3 different MN ribozyme species catalyzes the formation of another species from fragments provided as substrates, forming an autocatalytic cycle. Dotted and bold arrows show catalysis carried out by non-covalent and covalent ribozymes, respectively. Note that for clarity, only Watson-Crick IGS-tag

interactions are shown here. Any other non-Watson pair will have a weaker but non-zero activity (Extended Data Fig. 6c), therefore all networks possess some degree of autocatalysis. Top right panel: a simplified network representation shows catalytic species as nodes with their MN identity, and catalytic interactions as directed edges (corresponding to the dotted and bold black arrows of the bottom center panel). **b**, Random sets of ~3 droplets (small black disks), each containing different mixtures of WXY fragments, are fused by electrocoalescence in a microfluidic device with a droplet containing Z fragments and the reaction buffer (larger gray disks). This combinatorial process leads to a large diversity of catalytic networks, each contained in a different droplet (Methods). Substrate fragments are initially co-diluted with non-reactive hairpin RNA reporters that later allow the initial composition to be retrieved by sequencing. **c**, Droplet-level barcoded sequencing: each RNA-containing droplet is analyzed after incubation by fusing a sample of it to another droplet containing a hydrogel bead carrying DNA barcodes. These barcodes, specific to each bead, serve as primers for the reverse transcription of the RNAs, including the ribozymes formed during incubation, and the hairpin RNA reporters to identify initial condition. **d**, Compositional landscape of the 1837 unique measured networks[24]: Each ray is made of 16 boxes corresponding to the 16 possible MN species. A blank box means that the MN ribozyme is absent in this network, as determined from hairpin sequencing. Otherwise the box color indicates the measured fraction of the MN species. Grey arcs connect networks that differ from each other by a single node (addition or removal). **e**, Left: schematic of an *Azoarcus* network. Right: top, experimentally determined node fractions for the same network (error bars are ±1 s.d. over n=425 droplets); bottom, theoretical results with the kinetic model. **f**, Fraction obtained with the kinetic model versus measured fraction for every node that is a member of a 4 node-network. Bins with less than 10 points are discarded. Dark grey dots are mean values, quartile boxplots have 5th - 95th percentiles whiskers with flier points. The dotted grey line is the identity line. P-value < 0.001.

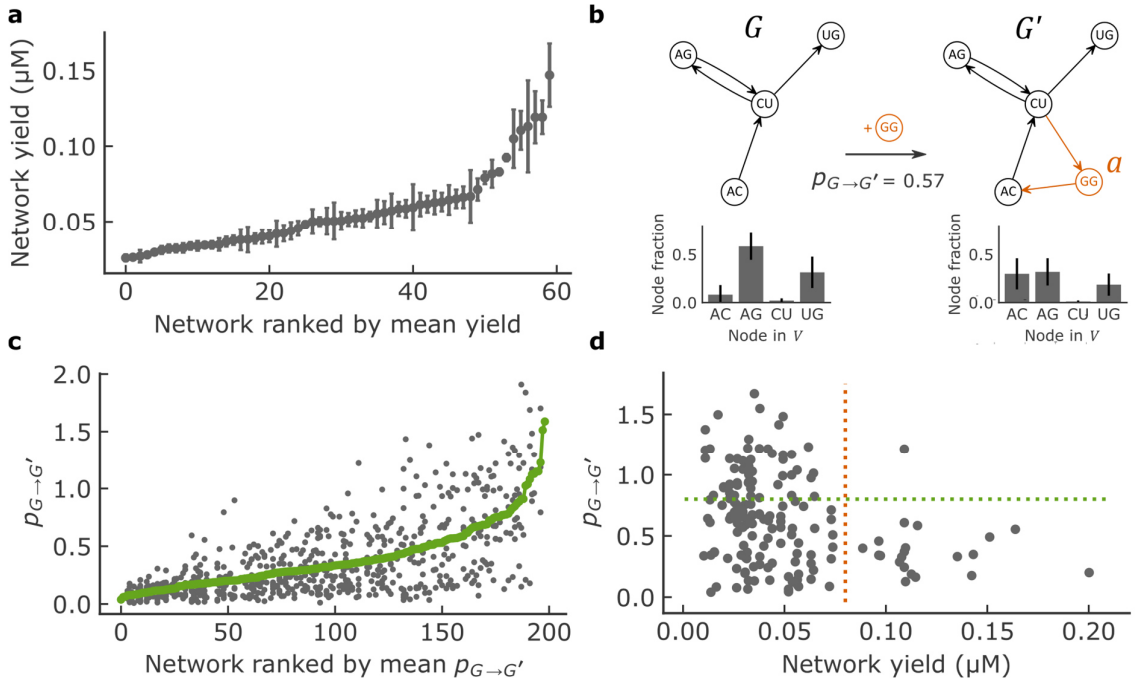

Fig. 2. Network growth and perturbation. a, Network total yield (concentration of WXYZ catalysts in μM) distribution of networks with four nodes and at least 10 replicates (for data on all sizes see Extended Data Table 2). Networks are ranked (x-axis) based on the mean across network replicates of the total WXYZ concentration (y-axis). The error bars show the Standard Error of the Mean. **b**, Example showing the addition of node a (GG, orange) to network G resulting in network G'. Top: schematic. Bottom: experimentally determined node fractions for the same network (error bars are ±1 s.d. over n=109 droplets (G) and n=15 droplets (G') **c**, Perturbation distribution of networks with four nodes. Networks are ranked (x-axis) based on the mean perturbation (y-axis). Each position on the x-axis corresponds to a certain network G, for which the perturbation has been computed for all possible single node additions present in the dataset, leading to several y-axis values corresponding to different G' networks. The green line is the average perturbation taken over all G' networks for each network G. **d**, Perturbation $p_{G\to G'}$ for networks with 3, 4 and 5 nodes plotted against network yield in μM for perturbations involving the addition of a novel catalysts (with G/C as IGS) with at least one target. The number of strongly perturbable ($p_{G\to G'}$>0.8, above the green dotted line) and high yield networks (>0.08 μM, right hand side of red dotted line) is very low compared to the null hypothesis of independence of perturbability and yield (one-sided Fisher exact test, N=162, odds ratio < 0.1, 95% confidence interval 0.01-0.66, p-value=$1.6.10^{-3}$).

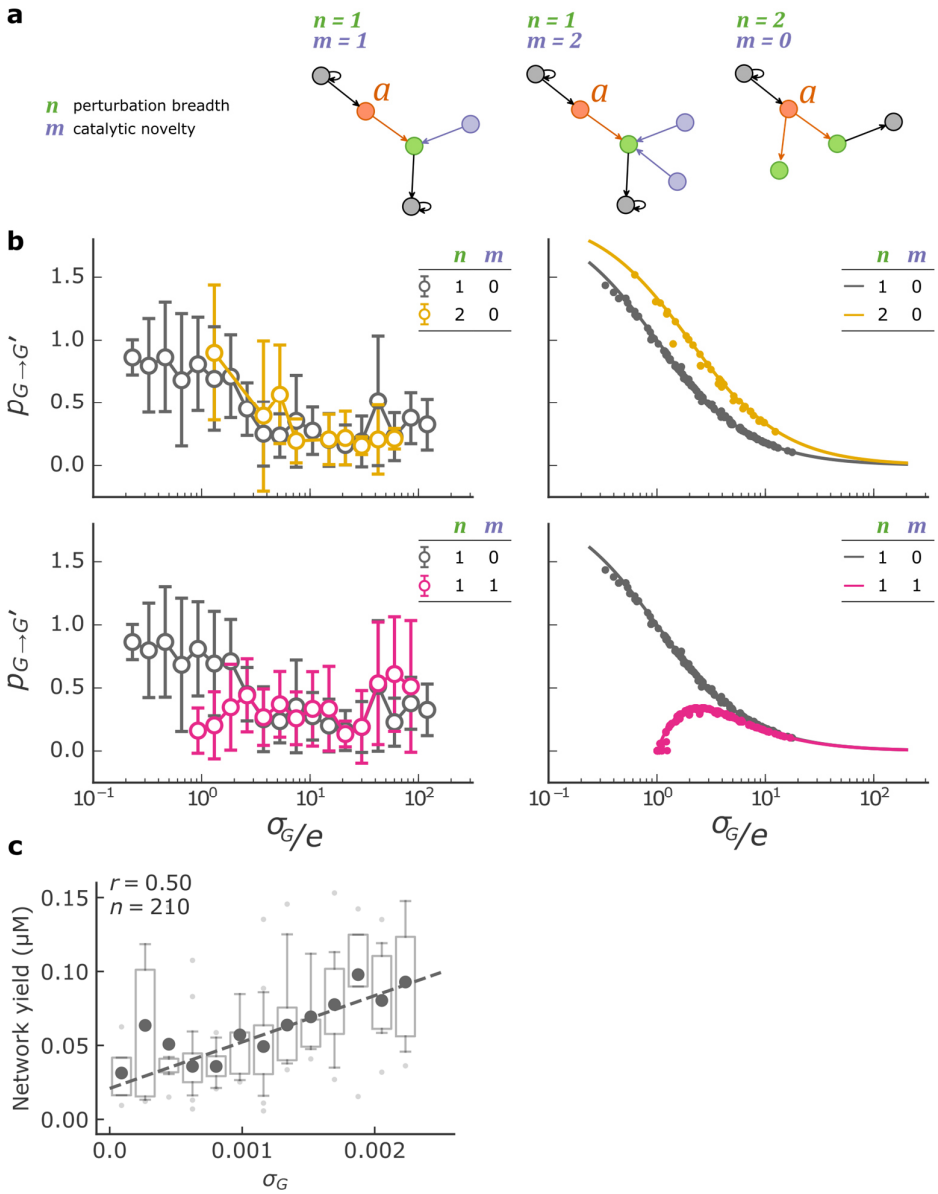

Fig. 3. Network perturbation analysis. a, Schematic of three situations where the parameters n, the number of targets of added node a, and m, the number of nodes sharing the same IGS as a, have different values. **b**, The perturbation $p_{G\to G'}$ is plotted against σ_G/e for different values of the parameters m and n for both the experimental data (left, mean and standard deviation per bin, bins with less than 3 points are discarded) and results predicted by in-degree centrality using the analytical expression (right, solid line) and with fractions predicted by eigenvector centrality (right, solid circles) for the networks with a number of nodes between 3 and 6 before addition. Results for other parameter values are shown in Extended Data Fig. 8. **c**, Network yield (μM) is plotted against σ_G for network with four nodes (see Methods for further details on how network yield is determined).

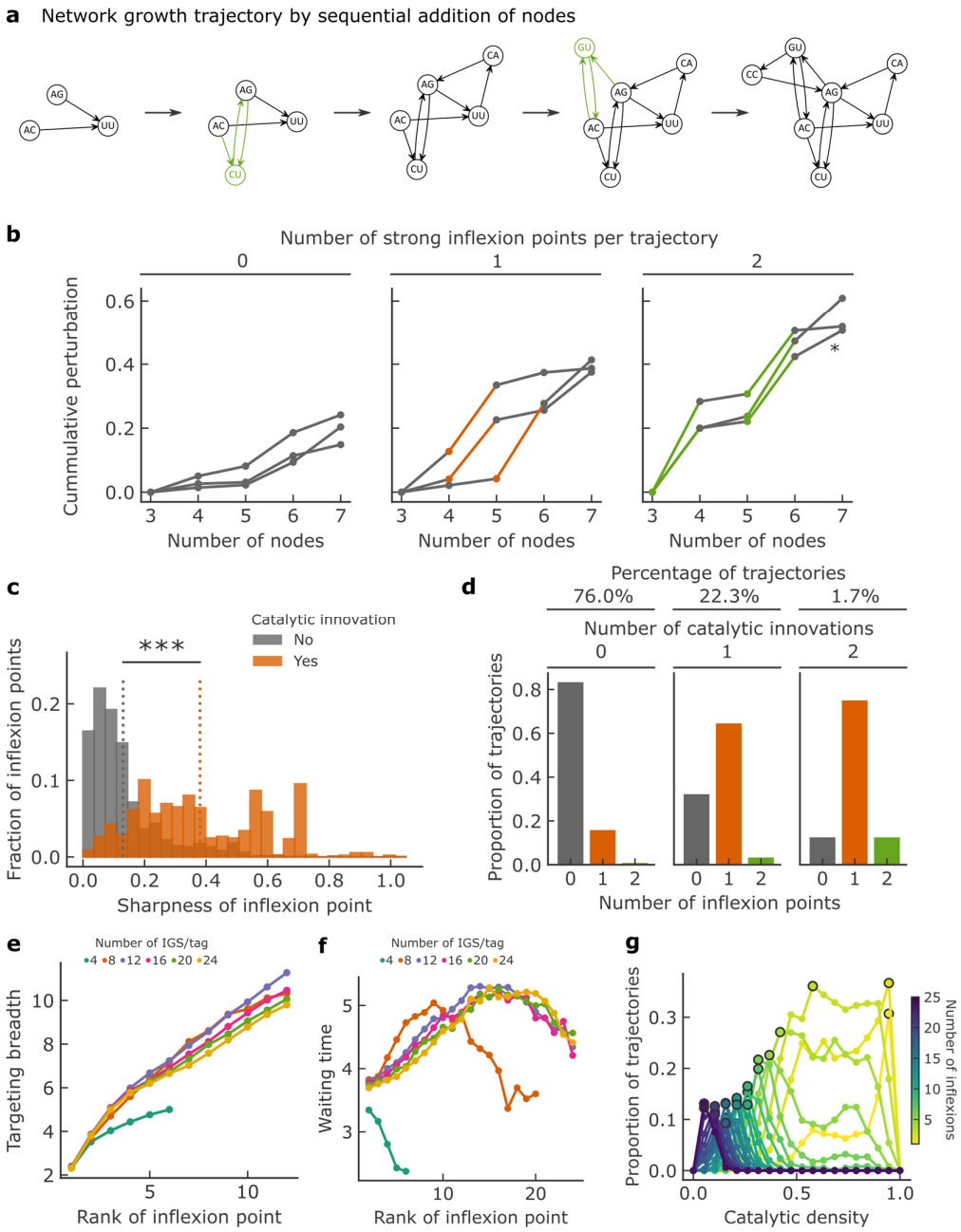

Fig. 4. Perturbation dynamics across network growth trajectories. a, Example of a network growth trajectory where at each step, a new node is added. Nodes resulting in strong perturbations (see panel b) are in green, and correspond to the IGS/tag pairs C-G and G-C. **b**, Examples of measured cumulative perturbation over trajectories, plotted against the number of node additions, by number of strong inflexions points (colored). The latter are determined as the top 25% in sharpness (absolute value of the third derivative, Extended Data Fig. 10a) measured over all trajectories. The asterisk (*) denotes the perturbation trajectory of the example shown in panel a. **c**, Distribution of sharpness for inflexion points associated with a catalytic innovation (orange, n=4,462) or not (grey, n=934). Catalytic innovations are defined as the introduction of strong IGS/tag interactions (CG or GC, Extended Data Fig. 6 b, c). that were not present until node addition. The dotted line is the mean of each distribution and the significance of the difference between the two distributions is reported (Mann–Whitney U test, $p < 0.001$). **d**, Distribution of the number of inflexion points within the 75th percentile sharpness per trajectory, depending on the number catalytic innovations per trajectory. **e-g**, Computational study of network growth trajectories for chemistries with varying number of IGS/tag pairs and with varying degrees of catalytic density points are

determined, as before, based on their sharpness (within the 75th percentile) here computed along a random sample of 1000 trajectories growing from 2 to 100 nodes. Catalytic densities are varied by random removal among the pool of all possible specific IGS/tag interactions. **e**, Targeting breath (number of targets) of catalysts causing strong perturbations, as the function of the inflexion rank. **f**, Waiting time (number of species additions) between two strong inflexions, as a function of the inflexion rank (e.g.: rank 5 is the fifth inflexion observed along a growth trajectory) **g**, Proportions of trajectories with a given number of strong inflexion points plotted against catalytic density for a chemistry comprising up to 24 different IGS/tag pairs.

351 ## Methods

352 **General material & methods.** All experiments used DNAse/RNase free water (Thermo Fisher
353 Scientific Product No.: 10977035). Chemicals were purchased from Sigma-Aldrich unless
354 specified otherwise. 4-(2-Hydroxyethyl)-1-piperazinepropanesulfonic acid (EPPS) was
355 purchased from Alfa Aesar (Product no.: J60511, CAS no.: 16052-06-5). Denaturing
356 polyacrylamide gels (12%) were prepared using gel stock solution (Roth, Product no.: A431.1)
357 and run in 1X Tris-Borate EDTA buffer. DNA/RNA oligonucleotides (Supplementary File 2)
358 were obtained from IDT DNA technologies.

359 **Transcription of RNAs.** RNAs were *in vitro* transcribed as described in[25], using DNA
360 templates produced as described in the Supplementary File 1. In the template for the WXY
361 fragments the IGS is duplicated at position 25 to allow identification by sequencing. The RNAs
362 were extracted with Phenol-Chloroform-Isoamyl alcohol, treated with DNase I (Thermo Fisher
363 Scientific, Product No.: EN0521) and purified on polyacrylamide gels. RNA concentrations
364 were measured using Qubit® RNA HS Assay Kit (Thermo Scientific, Product No.: Q32852).

365 **Microfluidic devices and set-up.** Droplet microfluidic experiments used HFE 7500 fluorinated
366 oil (3M™ Novec™, Product No.:98-0212-2928-5) and a fluorosurfactant (RAN
367 Biotechnologies, Product No.: 008-FluoroSurfactant). Devices were designed with AutoCAD
368 software (Supplementary File 4), printed at Selba SA. PDMS (polydimethylsiloxane) devices
369 were fabricated by soft-lithography as described in[26,27]. For electrocoalescence, indium tin
370 oxide coated glass slides were used (Delta Technologies, Product No.: CG-90IN-S215), with
371 channels containing 3 M NaCl liquid electrodes[28]. After plasma bonding, channels were made
372 hydrophobic with 2% 1H,1H,2H,2H-perfluorodecyltrichlorosilane (ABCR, Product No.:
373 AB111155) in HFE 7500. Droplet-based microfluidics experiments were performed using an
374 inverted microscope (Nikon Eclipse *Ti*) as described earlier[27]. Flows were controlled by either
375 syringe pumps (Harvard Apparatus Inc.) or by air-pressure control pumps (MFCS™-EZ,
376 Fluigent SA).

377 **Droplet microfluidic experiments**. The complete experimental system consists of the steps **A**
378 to **E** (Extended Data Fig. 1): (**A**) *Initial emulsions production:* Using all possible 16 WXY RNA
379 fragments ($_{gMg}WXY_{cNu}$)[18], 24 unique different WXY fragments combinations were prepared in
380 separate tubes (Extended Data Table 1). To determine those combinations, tube contents were
381 computationally drawn randomly among the 16 species. The total number of fragment types to
382 distribute over all tubes (with possible redundancies) was set to 50, which was computationally

383 found to maximize the number of distinct networks formed after random droplet fusions (10,000
384 iterations). Once this was fixed, network diversity was further maximized based on spectral
385 graph criteria, by selecting the fragment assignment (among 100,000 random realizations)
386 maximizing the Shannon entropy of the first eigenvalue and spectral gap distributions, across
387 networks resulting again from the simulation of 10,000 random droplet fusions.
388 Experimentally, for each combination, 1 μM of respective WXY fragment(s) was heated at
389 48°C and cooled down to room temperature over 10 min (0.1°C/sec) and mixed with hairpin
390 RNA reporter at a final concentration of 0.03 μM. All 24 mixes were encapsulated individually
391 in 5 pL droplets using flow focusing[29] on a dropmaker device (Supplementary File 4) using
392 flow rates of 100-150 μL/h for the aqueous (RNA) and 150-170 μL/h for the oil (HFE 7500
393 with 2% surfactant) phases, each emulsion being collected for 5 min. All 24 emulsions were
394 collected together in a 1.5 mL collection tube (with a PDMS cap) containing oil with 2%
395 surfactant and mixed thoroughly. A 1.6 μM solution of Z RNA fragment in 1X *Azoarcus*
396 reaction buffer (30 mM EPPS pH 7.4, 20 mM $MgCl_2$), was folded in the same manner as WXY
397 RNA, and encapsulated in 50 pL droplets using a 50 pL drop-making device (Supplementary
398 File 4), at flow rates of 350 μL/h for the aqueous (RNA) and 250 μL/h for the oil (HFE 7500
399 with 2% surfactant) phases, droplets being collected in a 0.5 mL collection tube (with a PDMS
400 cap). All flows were driven by syringe pumps. (**B**) <u>*Electrocoalescence of initial emulsions*</u>: The
401 5 pL droplets (containing WXY fragments) and 50 pL droplets (containing Z fragment and
402 reaction buffer) were re-injected into separate channels of a droplet fusion device
403 (Supplementary File 4). Both 5 pL and 50 pL droplets were spaced using HFE 7500 oil
404 containing 2% surfactant and brought together into the same channel, where they were
405 electrocoalesced[19,28] using an AC electrical field (Agilent 33522A waveform generator, sine
406 function, 4 kHz, 400 mV, 50 Ω) amplified 10^3 times (TREK high-voltage amplifier). Flows
407 were regulated such that, on average, between one and five 5 pL droplets coalesce with one 50
408 pL droplet (Supplementary File 5). This resulted in ~1/10th dilution of WXY RNA concentration
409 in the fused droplets (the Z fragment is in stoichiometric excess). All flows were driven by a
410 pressure control system (MFCS™-EZ, Fluigent SA), and the desired fusion frequency achieved
411 by carefully adjusting and coupling the flows with pressure values of 380-400, 350-380, 470-
412 520 mbar for 50 pL droplet emulsion, 5 pL droplet emulsion and spacer oil channel,
413 respectively. Electrocoalescence and collection (in a 0.2 mL tube with a PDMS cap) was
414 performed for ~ 3.5 h and the emulsions were stored on ice during the entire process. To monitor
415 the fusion frequency during the collection, fusion events were counted from videos recorded
416 every 20 min, showing very stable fusion frequency, closely comparable to what was obtained

417 by sequencing hairpin RNA reporters (Extended Data Fig. 4). (**C**) *Incubation and splitting of*
418 *droplets:* After collection, fused droplets were incubated at 48°C in a thermo-block for 1 h to
419 allow the accumulation of ribozymes. In order to dilute the $MgCl_2$ during the reverse
420 transcription (RT) step, these droplets (~60-65 pL) were re-injected (spaced with HFE 7500 oil
421 containing 2% surfactant) and split by a T-junction device[30] (Supplementary File 4) into smaller
422 droplets (~5 pL) prior to the RT step. Flow rates were maintained using pressures of 800-1000
423 mbar and 150-250 mbar, respectively for the oil separator channel and droplet inlet. (**D**) *Droplet*
424 *barcoding and RT in droplet*: To sequence the RNA in each split droplet we developed a
425 strategy combining droplet barcoding and RT in droplets, inspired by single-cell
426 transcriptomics methods described earlier[20,31]. Here barcoded hydrogel beads are individually
427 encapsulated in droplets with all the necessary reagents for RT and fused with RNA network
428 containing droplets. The details of each step are as follows: (*a) Barcoded hydrogel bead*
429 *synthesis*: Hydrogel beads were produced by co-encapsulating 10% (w/w) polyethylene glycol
430 diacrylate (PEG-DA) 6000 (Sigma, Product No.: 701963), 1% (w/w) PEG-DA-700 (Sigma,
431 Product No.: 455008), 400 µM of acrydite-modified dsDNA with a 4 base sticky-end (Oligo
432 10, top, carrying a 5'-acrydite modification, and Oligo 11, bottom, Supplementary File 2), 10
433 µM of FITC-Na (Fluorescein isothiocynate), 1% (v/v) photo-initiator (2-hydroxy-2-
434 methylpropiophenone, Sigma, Product No.: 405655) in buffer (75 mM Trizma HCl pH 7.4, 50
435 mM NaCl) using flow focusing[32] on a dropmaker device (Supplementary File 4). 9 pL droplets
436 were produced using flows of 150 µL/h for aqueous solution and 500 µL/h for oil (HFE 7500
437 with 2% surfactant). Droplets were polymerized by UV irradiation (UV omnicure AC475-365,
438 Lumen Dynamics, ~360 mW exposure, λ_{nm} = 365 nm) through a PTFE tubing and collected in
439 5 mL tube (tubing internal diameter = 0.3 mm, distance from lamp 3 cm, tubing length = 12
440 cm; approximate exposure time = 47 s). Prior to UV irradiation, the complete experiment set-
441 up was maintained in the dark to avoid any spontaneous polymerization. The collected droplets
442 were washed once with 4 mL hexane to break the emulsion and then the beads washed 3 times
443 with 4 mL binding-wash buffer (20 mM Trizma-HCl pH 7.4, 50 mM NaCl, 0.1% of Tween 20)
444 by centrifuging at 3000 g for 2 min. Beads were then filtered using Steriflip 20 µm Nylon filters
445 (Millipore, Product No.: SCNY00020) and stored in binding-wash buffer supplemented with 1
446 mM EDTA. In contrast to earlier methods[20,31], barcodes were built on the beads using a split-
447 and-pool ligation strategy[33] (Extended Data Fig. 2). For this, 250 µL (~10 million) of pelleted
448 beads were washed 3 times with 4 mL of binding-wash buffer by centrifuging at 3000g for 2
449 min, and were subjected to a first ligation step. Ligation was performed on a 2 mL reaction
450 scale with 1X T7 DNA Ligase buffer (New England Biolabs), 4 µM dsDNA adaptor with two

451 different 4 base sticky-ends, the first being complementary to the 4 base sticky-end on the
452 beads, and containing a BclI restriction site and the Read 2 illumina adaptor sequence (Oligo
453 12, top and Oligo 13, bottom, Supplementary File 2), 30 U/µL of T7 DNA Ligase (New England
454 Biolabs, Product No.: M0318L), at room temperature for 25 min with agitation at 600 rpm.
455 Beads were then washed 5 times with 4 mL of binding-wash buffer and pelleted after the last
456 wash. For the next ligation step, a master-mix (1.6 mL) was prepared to containing 1X T7 DNA
457 Ligase buffer, 30 U/µL of T7 DNA Ligase and divided into the wells of a 96-well deep well
458 plate (16 µL per well), pre-filled with 4 µL of 20 µM 1st barcode index (Index A)
459 (Supplementary File 2), with a different index in each well. These indexes had two different 4
460 base sticky-ends, the first being complementary to the free sticky-end of oligos ligated in
461 previous step (dsDNA, Oligo 12 and 13). The plate was sealed and incubated at 25°C with 600
462 rpm for 25 min. Then the ligase was heat inactivated at 65°C for 10 min and the content of all
463 the wells was pooled after adding 200 µL of binding-wash buffer containing 1 mM EDTA.
464 After pooling, the beads were washed 7 times with 4 mL of binding-wash buffer. The complete
465 process of split-and-pool was repeated to ligate the 2nd (Index B) and 3rd (Index C) barcode
466 indexes (Supplementary File 2) generating a total diversity of 8.8 x 10^5 (96^3) barcodes. After
467 the final pooling step, a partially double-stranded sequence was ligated to all the beads using
468 the same ligation protocol (Oligo 14, top and Oligo 15, bottom, Supplementary File 2). This
469 sequence comprises a sticky-end complementary to the free sticky-end on the 3rd index, and a
470 single-stranded 33 base long 3'-overhang at the other end (Extended Data Fig. 2b). Out of these
471 33 nucleotides, the first 8 are random nucleotides used as unique molecular identifiers (UMIs)[34]
472 and remaining 25 nucleotides, which function as a primer for RT, are complementary to the 3'
473 end of the WXYZ ribozyme and hairpin RNA reporter (both contain the same primer binding
474 region). The final barcoded hydrogel bead library was washed 5 times with 4 mL of binding-
475 wash buffer supplemented with 1 mM EDTA and re-suspended in the same buffer. (b)
476 *Encapsulation and fusion*: The barcoded beads (50 µL) were washed 5 times with 500 µL of
477 binding-wash buffer by centrifuging at 11866 g for 1 min. Washed beads were then mixed with
478 2.5 µL of 10 mM dNTPs, 10 µL of 5X SuperScript III reaction buffer (Invitrogen), 2.5 µL of
479 100 mM dithiothreitol (DTT), 0.4% of Tween20 (10%), 100 units of SUPERase·In™ inhibitor
480 (Thermo Fisher Scientific, Product No.: AM2694) and incubated at 37°C for 30 min to ensure
481 diffusion of all reactants within the beads. After this, the beads were centrifuged as above and
482 excess of liquid over the beads was removed. Then, at 4°C, 500 units of reverse transcriptase
483 (SuperScript III, Thermo Fisher Scientific, Product No.: 18080044) and 25 units of BclI
484 restriction enzyme (New England Biolabs, Product No.: R0160L) were added to the beads and

485 mixed thoroughly. These hydrogel beads together with the other reagents were encapsulated
486 individually in ~50 pL droplets (Supplementary File 6), fused with RNA droplets on the same
487 microfluidic device (Supplementary File 4). The injection of close-packed deformable beads
488 resulting in >99% of droplets containing a single barcoded hydrogel bead. The 5 pL RNA
489 containing droplets and the 50 pL bead containing droplets were fused at a 1:10 ratio to ensure
490 that, in the majority of cases, no more than one of the formers is fused with one of the latter.
491 For this, flows were pressure controlled using, respectively, 550, 225, 650, 450 mbar for
492 hydrogel beads, 5 pL droplets, oil to control droplet spacing (HFE 7500 with 2% surfactant)
493 and oil for beads encapsulation (HFE 7500 with 2% surfactant). Electrocoalescence was
494 performed as described above. Fused droplets were collected in 0.2 mL collector tube (with
495 PDMS cap) containing oil with 2% surfactant. (c) *cDNA synthesis and extraction*: The fused
496 droplets were then incubated at 60°C in a thermo-block for 1 h to release the DNA barcodes
497 using the BclI restriction enzyme and perform cDNA synthesis in droplets. The emulsion was
498 broken post incubation by adding 2 volumes of 1*H*, 1*H*, 2*H*, 2*H*-Perfluoro-1-octanol and 100
499 µL water. The pooled barcoded cDNAs are then isopropanol precipitated and re-suspended in
500 40 µL of water. **(E)** <u>*Sequencing sample preparation*</u>: In order to block extension of the non-
501 elongated primers, 20 µL of cDNA was mixed with 1X TdT reaction buffer (New England
502 Biolabs), 0.25 mM $CoCl_2$, 0.4 mM ddCTP (Roche CustomBiotech, Product No.: 12158183103)
503 and 0.4 U/µL of Terminal Transferase (TdT, New England Biolabs, Product No.: M0315L).
504 The reaction was carried out in 50 µL volume and incubated for 30 min at 37°C before heat
505 inactivation at 70°C for 10 min. The TdT treated cDNAs were purified using magnetic beads
506 (AMPure XP, Beckman Coulter, Product No.: A63881) following the manufacturer's protocol.
507 Sequencing adaptors were then appended using two sequential PCR steps (Extended Data Fig.
508 3a). The first PCR was performed in multiples of 20 µL volume where 2 µL of TdT treated
509 reverse transcription reaction was mixed with 0.5 µM of Oligo 16 (also containing a 6
510 nucleotide stretch used as sample barcode to multiplex different samples for the sequencing
511 run) and 0.5 µM of Oligo 17 (Supplementary File 2) as forward and reverse primers in 1x PCR
512 buffer (Thermo Scientific), 0.2 mM dNTPs, 0.01 U/µL of polymerase (Thermo Scientific
513 Phusion Hot Start II, Product No.: F459) using the following protocol: initial denaturation
514 98°C/30sec, then 18 cycles of denaturing 98°C/10 s, annealing and extension 72°C/1 min, and
515 a final extension of 72°C/5 min. PCR products were purified using AMPure XP magnetic beads
516 and eluted in 34 µL of water. The second PCR was performed as above, but in 40 µL volume
517 with 4 µL as PCR I purified product as template, using Oligo 18 and Oligo 19 (Supplementary
518 File 2) as forward and reverse primers, and using the following protocol: initial denaturation

519 98°C/30sec, then 10 cycles of denaturing 98°C/10 s, annealing 56°C/30 s, extension 72°C/30
520 s, and a final extension of 72°C/5 min. The final sample was purified using AMPure XP
521 magnetic beads, resuspended in 34 µL of water, analysed on TapeStation (Agilent 2200
522 TapeStation, using high sensitivity D1000 ScreenTape®, Product No.: 5067-5584) and
523 quantified by Qubit® dsDNA HS Assay Kit (Thermo Scientific, Product No.: Q32854).
524 Libraries were sequenced using the Illumina NextSeq 550 system in 2*150 High Output mode
525 at the Genotyping and Sequencing Core Facility, ICM Paris (iGenSeq, Institut du cerveau et de
526 la moelle épinière).

527 **Sequencing data processing**. Custom software was written to process sequencing data and
528 further data analysis steps. The libraries were sequenced in paired-end mode with read 1 and
529 read 2 of 180 bp and 120 bp, respectively. Read 1 was used to determine the sample barcode
530 (used for multiplexing samples for sequencing) and the RNA molecule identity (either an
531 *Azoarcus* ribozyme with specific IGS-tag pair or a hairpin RNA reporter). Read 2 was used to
532 determine the UMIs[34] and the droplet barcode. The structure of read 1 and 2 is summarized in
533 Extended Data Fig. 3b. *UMI normalization*: Four meta fields were associated for each pair of
534 reads: sample barcode, droplet barcode, UMI and RNA molecule identity (details in
535 Supplementary File 1). Reads missing any of these were discarded (~30%). The reads with the
536 same meta information were merged and the read count was added as an extra meta field. This
537 allows to filter out noise due to sequencing errors, given that read counts resulting from such
538 errors are significantly lower (threshold indicated on Extended Data Fig. 3e). The filtering
539 thresholds for the minimum number of reads per UMI were determined separately for the
540 *Azoarcus* ribozymes and hairpin RNA reporters based on the shape of the distribution of number
541 of reads per UMI (Extended Data Fig. 3e-f). *Final data processing*: Filtered UMI-normalized
542 reads were then clustered by droplet barcode to count the number of UMIs per type of RNA
543 molecule per droplet barcode (Extended Data Fig. 3f). For each droplet barcode, only hairpin
544 RNA reporters where UMIs made up ≥7.5% of the total of hairpin UMIs were retained. This
545 threshold value was set to optimally match the fusion distribution measured by video (Extended
546 Data Fig. 3g). Within each droplet, ribozyme sequences that did not corresponding to a correct
547 hairpin reporter were discarded. Then, only the droplet barcodes with more than 10 UMIs
548 associated with hairpin RNA reporters and 20 with ribozymes were retained and the fraction of
549 each node in the network was computed. As before, these thresholds were chosen to closely
550 match the observed distribution of drop fusion determined from videos acquired during the
551 experiments (Extended Data Fig. 3h, i). Processed network compositions and mean node

552 fractions are publicly available for all unique networks (Supplementary File 3). To determine
553 network yield per droplet, first we computed a droplet-specific UMI to concentration
554 conversion rate by considering total hairpin reporter UMIs as well as number of different
555 hairpin reporters identified. This was then used to convert total number of ribozyme UMIs into
556 a yield value.

557 **Controls for droplet-level sequencing biases.** Four 5 pL emulsions (A, B, C and D) were
558 prepared, each with: a distinct pair of hairpin RNA reporters at a final concentration of 5 nM, a
559 set of 4 WXYZ ribozymes with the same IGS but in different proportions (total concentrations
560 summing to 100 nM) and 1.6 μM of Z fragment. The four emulsions were mixed and then
561 singly fused to droplets containing hydrogel beads as described above to perform droplet level
562 sequencing. The data was processed as above using the same thresholding strategy. We
563 quantified the bias as the proportion of droplets containing pure (A, B, C or D) and compared
564 to mixed populations (AB, AC, AD, BC, BD, CD, ABC, ABD, BCD and ABCD, Extended
565 Data Fig. 5d).

566 **Experimental measurement of catalysis by non-covalent and covalent ribozymes.** Self-
567 assembly of *Azoarcus* ribozymes with different IGS/tag pairs were re-measured in 20 mM
568 $MgCl_2$, using the strategy developed by von Kiedrowski[35], as described[21]. For this, the initial
569 rate of formation of WXYZ from WXY and Z fragments was measured as a function of the
570 concentration of doped covalent WXYZ ribozymes (with same IGS and tag as the WXY
571 fragment). The concentration of RNA fragments were identical to the droplet experiments (0.1
572 μM of WXY fragment and 1.6 μM of Z fragment) with additional but minor amounts (0.001
573 μM) of WXY fragment, radiolabeled using T4 Polynucleotide Kinase (New England Biolabs)
574 and γ-32P ATP (Perkin-Elmer). In accordance to previous measurements[21], the initial rate of
575 formation of WXYZ (v_0) was found to depend linearly on the concentration of the doped
576 WXYZ. This linear relationship can be described with the following linear equation $v_0 = \alpha x +$
577 β (Extended Data Fig. 6 b,c) where, x is the concentration of the covalent ribozyme, α is the
578 slope for an IGS/tag pair, which quantifies the WXYZ synthesis by covalent ribozymes, and β
579 is the y-intercept, which quantifies the WXYZ synthesis by non-covalent ribozymes (trans-
580 catalysis by non-covalent complex of WXY and Z fragments)[18]. Wobble pairs (GU and UG)
581 and one of the mismatched IGS/tag pairs (AG) were also measured and found to have negligible
582 values for α and β.

583 **Kinetic model.** In a network, covalent catalysts from species j, whose concentration is x_j,
584 contributes to the rate of formation of covalent catalysts from species i with the term $\alpha_{ij}x_j$

while non-covalent catalysts contribute with the constant term β_{ij}. α_{ij} and β_{ij} terms were measured experimentally and independently from the network experiments, for single IGS-tag pairs (Extended Data Fig. 6b-c). The production rate of each species is $\dot{x}_i = \sum_j \alpha_{ij} \cdot x_j + \beta_{ij}$, resulting in a linear system of ordinary differential equations for each network depending on the IGS-tag combinations provided from the RNA fragments.

Additional references

25. Arsene, S., Ameta, S., Lehman, N., Griffiths, A. D. & Nghe, P. Coupled catabolism and anabolism in autocatalytic RNA sets. *Nucleic Acids Res*. **46**, 9660-9666 (2018).
26. Duffy, D. C., McDonald, J. C., Schueller, O. J. & Whitesides, G. M. Rapid Prototyping of Microfluidic Systems in Poly(dimethylsiloxane). *Anal*. *Chem*. **70**, 4974-4984 (1998).
27. Mazutis, L. et al. Single-cell analysis and sorting using droplet-based microfluidics. *Nat*. *Protoc*. **8**, 870-891 (2013).
28. Sciambi, A. & Abate, A. R. Generating electric fields in PDMS microfluidic devices with salt water electrodes. *Lab Chip* **14**, 2605-2609 (2014).
29. Anna, S. L., Bontoux, N. & Stone, H. A. Formation of dispersions using "flow focusing" in microchannels. *Appl*. *Phys*. *Lett*. **82**, 364-366 (2003).
30. Link, D. R., Anna, S. L., Weitz, D. A. & Stone, H. A. Geometrically mediated breakup of drops in microfluidic devices. *Phys*. *Rev*. *Lett*. **92**, 054503 (2004).
31. Macosko, E. Z. et al. Highly Parallel Genome-wide Expression Profiling of Individual Cells Using Nanoliter Droplets. *Cell* **161**, 1202-1214 (2015).
32. Anna, S. L., Bontoux, N. & Stone, H. A. Formation of dispersions using "flow focusing" in microchannels. *Appl*. *Phys*. *Lett*. **82**, 364-366 (2003).
33. Grosselin, K. et al. High-throughput single-cell ChIP-seq identifies heterogeneity of chromatin states in breast cancer. *Nat*. *Genet*. **51**, 1060-1066 (2019).
34. Kivioja, T. et al. Counting absolute numbers of molecules using unique molecular identifiers. *Nat*. *Methods* **9**, 72-74 (2011).
35. von Kiedrowski, G. A Self-Replicating Hexadeoxynucleotide. *Angew*. *Chem*. *Int*. *Ed*. *Engl*. **25**, 932 (1986).

Extended Data

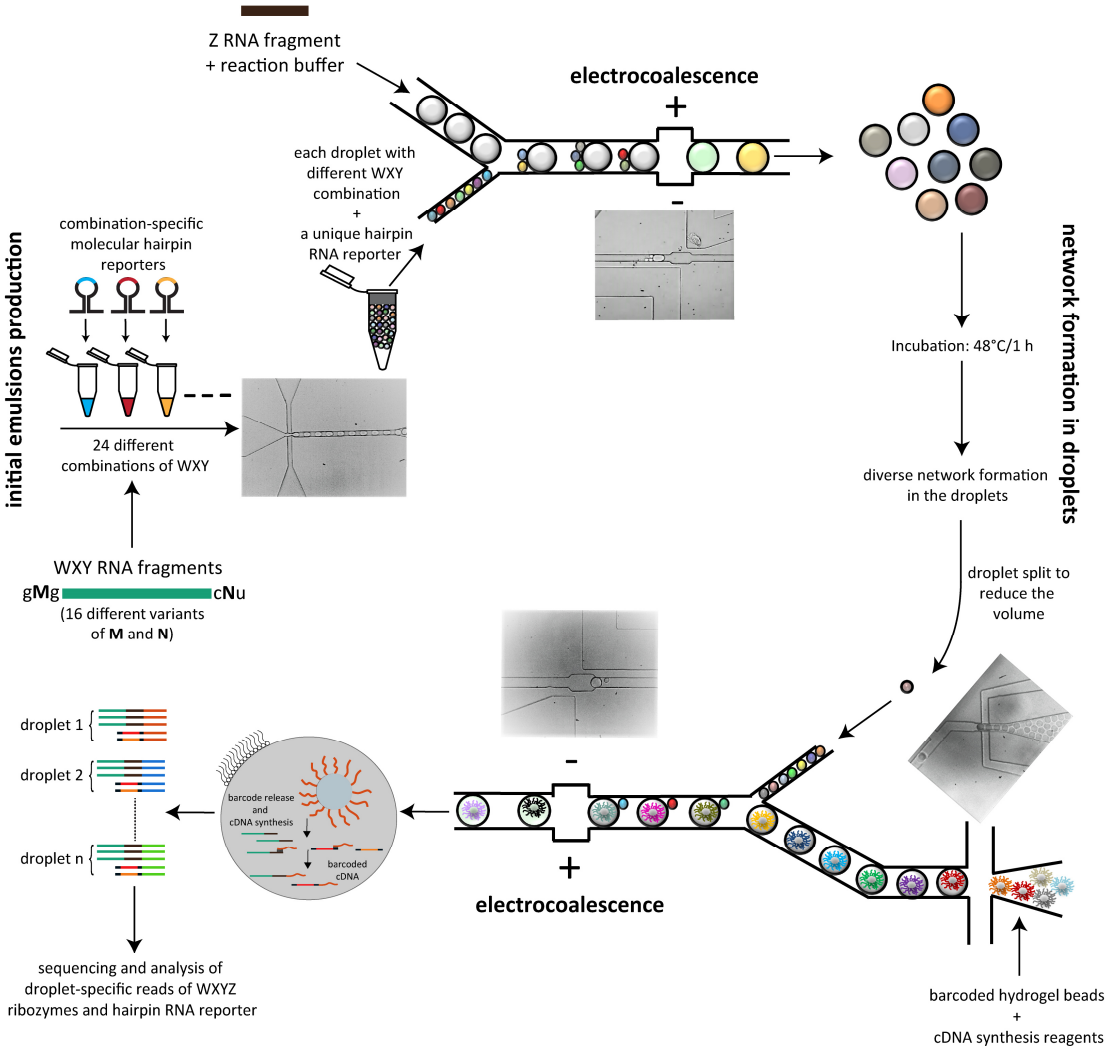

Extended Data Fig. 1. Schematic of the complete experimental set-up. The different steps involved in the experiment. See Methods for details. On a first microfluidic device, 24 different initial emulsions, comprising 5 pL droplets, were prepared, each containing a unique combination of WXY fragments (Extended Data Table 1), and a unique molecular hairpin RNA reporter. These emulsions were collected in a single tube (1.5 mL) and mixed thoroughly. These 5 pL droplets were then re-injected into a second microfluidic device, where they were fused by electrocoalescence with 50 pL droplets, produced on a separate chip, containing Z fragment and the reaction buffer. The pairing of 5 pL and 50 pL droplets was controlled such that one to five 5 pL droplets fuse with one 50 pL droplet. After fusion, the resulting emulsion, comprising 65 pL droplets, was incubated at 48°C for 1 h, and then split into 5 pL droplets on a third microfluidic device to reduce the volume. These droplets were re-injected into a fourth microfluidic device, where they were fused with 50 pL droplets, produced on the same chip, containing single hydrogel beads carrying barcoded cDNA primers, and reverse transcription reaction reagents. The ratio of 5 pL to 50 pL droplets was kept low (1:10) such that only one 5 pL RNA droplet was fused with one 50 pL droplet. The resulting emulsion was incubated at 60°C for 1 h to allow release of barcoded primers from the beads and cDNA synthesis. Then, the emulsion was broken, the barcoded cDNA was amplified by PCR to append sequencing adaptors, and sequenced.

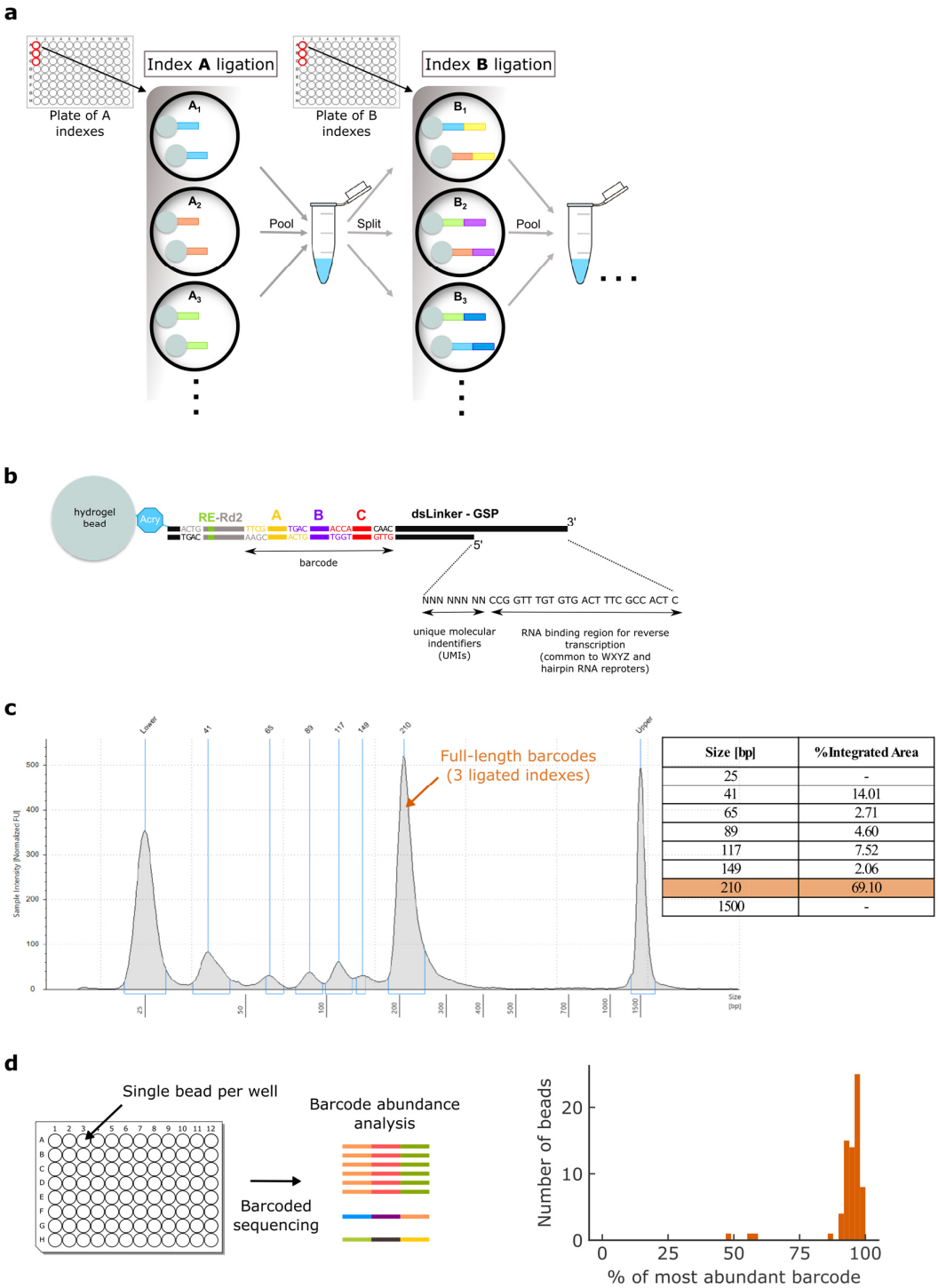

Extended Data Fig. 2. Barcoded hydrogel beads. a, Synthesis of barcoded hydrogel beads using a split and pool ligation strategy (details in Methods). On each bead, the clonal population of barcodes is built by successive ligation of indexes in one of the wells of 3 successive 96-well plates, in which each well contains a different index. Between each ligation step, beads are pooled before being distributed randomly in the 96 wells of the next plate. After the ligation of three indexes (A, B and C), a common oligo containing a linker (double stranded), UMIs (8 nt, single stranded), and the RNA binding region for reverse transcription (25 nt, single stranded) is ligated. **b**, Final structure of a barcode: linker, restriction site (RE), Read 2 Illumina sequence (Rd2), 3 barcode indexes (A, B and C) separated by linker regions, UMI and cDNA primer. The sequences of the ligated 4 base sticky-ends in the linker regions are indicated. **c**, Capillary electrophoresis (TapeStation, Agilent) data of the barcoded primers released from beads by restriction digestion. The length at the main peak (~70%) corresponds to fully ligated

645 barcodes with three indexes. Note that the actual length of full barcodes is 152 bp compared to the length indicated
646 by TapeStation (210 bp) due to barcodes being partially single-stranded. See Supplementary File 1 for details. **d**,
647 Distribution of percentage of the most abundant barcode sequence per bead is plotted for n=71 beads obtained by
648 sequencing of barcodes released from single beads in microplate wells. See Supplementary File 1 for details.
649

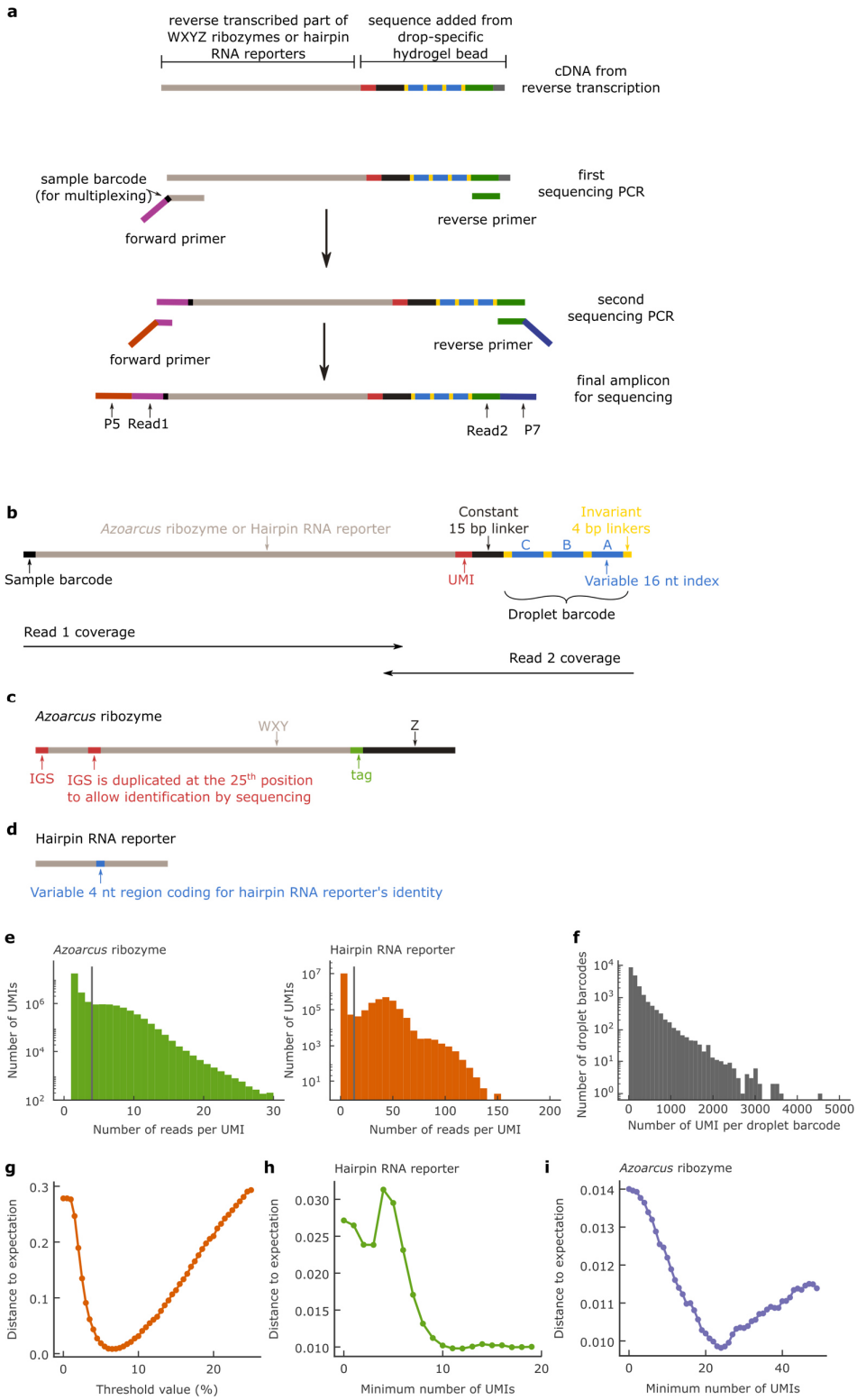

Extended Data Fig. 3. Sequencing and analysis. a, Schematic of PCR steps to append sequencing adaptors (see Methods). In the first step, barcoded cDNAs are amplified with a gene-specific forward primer, which also contains a barcode for multiplexing different samples for sequencing, and a common read 2 reverse primer. The PCR products from first PCR are then subjected to a second PCR to add adaptors compatible with Illumina sequencing platforms. **b-c**, Sequencing read structures **b**, Generic paired-end read structure. **c**, Detailed structure of the reads

657 for *Azoarcus* ribozymes and for hairpin RNA reporters. **d**, Structure of molecular hairpin RNA reporters, which
658 share the same 5' and 3' regions as WXYZ to allow amplification. These hairpins have a variable loop region of
659 4 nucleotide serving as barcode. **e**, Distribution of number of UMIs as a function of the number of reads per UMI
660 for reads associated with *Azoarcus* ribozymes or hairpin RNA reporters. The threshold, indicated by the gray line,
661 is determined by the intersection of the the "noise" distribution with very low number of reads per UMI and the
662 "signal" distribution with higher mean number of reads per UMI. Any UMIs with less reads than this threshold
663 were discarded. Note that x-axis scale for the plots is different because of the more efficient amplification of
664 hairpin reporters during PCR due to their smaller size. **f**, Distribution of number of UMIs (ribozyme and hairpin)
665 per droplet barcode. **g-i**, Choosing the thresholds. The distance to expectation is the Euclidian distance between
666 the distribution of the number of hairpin RNA reporters per droplet barcode once the three thresholds (see below)
667 have been applied, and the distribution of droplets at the fusion step measured by video acquisition. The three
668 thresholds are: **g**, the minimum percentage of total hairpin RNA reporter UMIs used to declare the corresponding
669 hairpin reporter to be part of the coding set for a given droplet barcode (chosen value = 7.5%), **h**, the minimum
670 number of hairpin RNA reporter UMIs for a droplet barcode to be included in the final dataset (chosen value =
671 10), and **i**, the minimum number *Azoarcus* ribozyme UMIs for a droplet barcode to be included in the final dataset
672 (chosen value = 20).

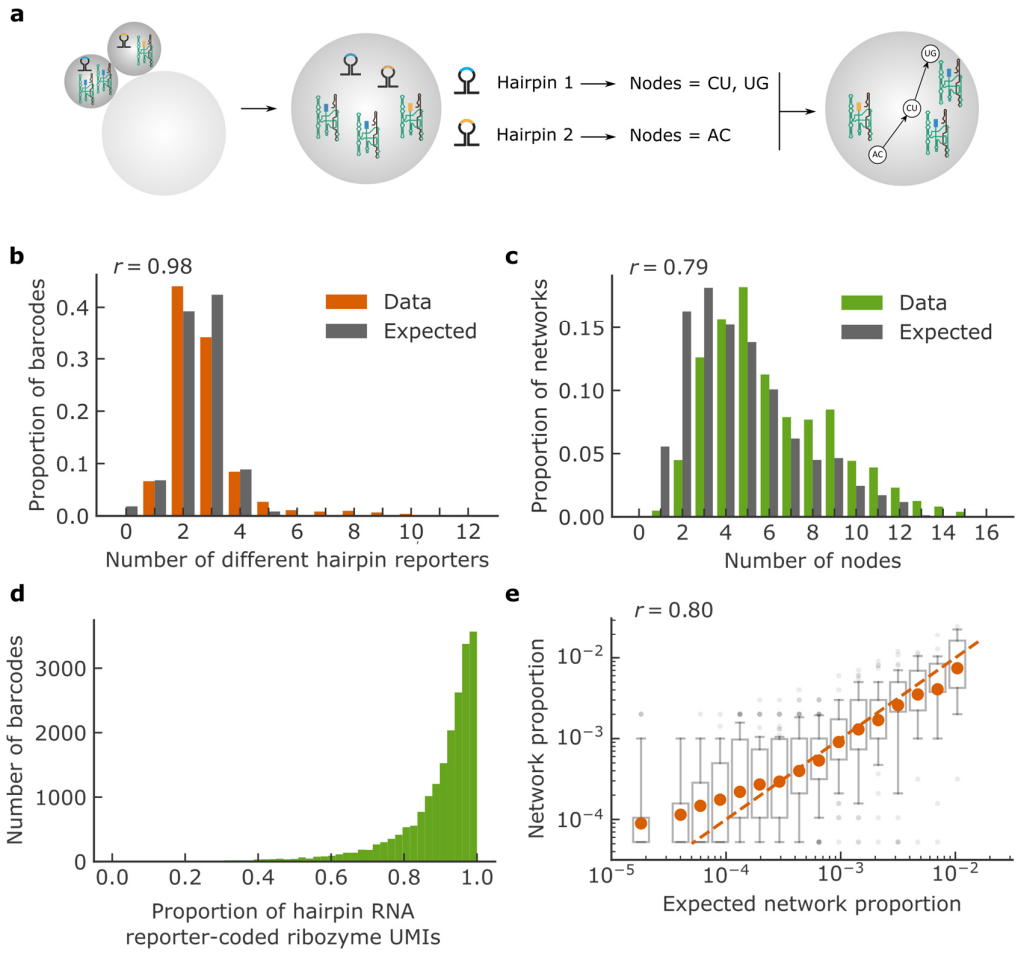

Extended Data Fig. 4. Identification of the network structure at the droplet level using hairpin RNA reporters. a, Schematic illustrating identification of a network structure using hairpin RNA reporters. The hairpin RNAs where the UMI counts make up ≥7.5% of the total number of UMI counts for hairpin RNAs are considered as part of the coding set. This can be used to derive network structure in addition to node identification using an internal mutation in WXYZ ribozyme (Extended Data Fig. 3c, Supplementary File 1). The number of UMIs for each node of the identified network structure gives the node fraction. **b**, In orange, measured distribution of the number of hairpin RNA reporters per droplet barcode in the final dataset. In dark grey, distribution of number of 5 pL droplets (containing initial WXY emulsions) fused with a 50 pL droplet (containing reaction buffer and Z) measured by video acquisition (Methods). Pearson's correlation coefficient is reported ($p<0.001$, $n=13$). **c**, In green, distribution of number of nodes per network per droplet barcode in the final dataset. In dark grey, expected distribution from simulating the library fusion step with the same number of droplets as in the data and with the fusion frequencies measured by video acquisition (Methods). Pearson's correlation coefficient is reported ($p<0.001$, $n=17$). **d**, Histogram of distribution of the proportion of hairpin RNA reporter-coded ribozyme UMIs, defined as the ratio between the total numbers of UMIs associated with nodes identified by the hairpin reporters and the total number of UMIs for *Azoarcus* ribozyme identified by the internal mutation (Supplementary File 1) for the same droplet barcode. A value of 1 is reached when all ribozyme UMIs predicted by the set of hairpin reporters are identified. **e**, Correlation between the measured and expected network proportions. Network proportion is calculated as the ratio between the number of replicates of a given network and the total number of replicates for all networks. Expected network proportion is obtained by simulating the library fusion step with 50,000 droplets mimicking the experimental set-up using the fusion frequencies measured by video acquisition. About 1/3 of the networks in the data do not have any replicate in the simulation and are excluded from the analysis. Bins with less than 10 points were discarded. The box extends from the lower to upper quartile values of the data, with a dot at the mean. The whiskers extend from the 5th percentile to the 95th. Flier points are those past the end

of the whiskers. The dotted orange line is the identity line. Pearson's correlation coefficient is reported ($p<0.001$, $n=2160$).

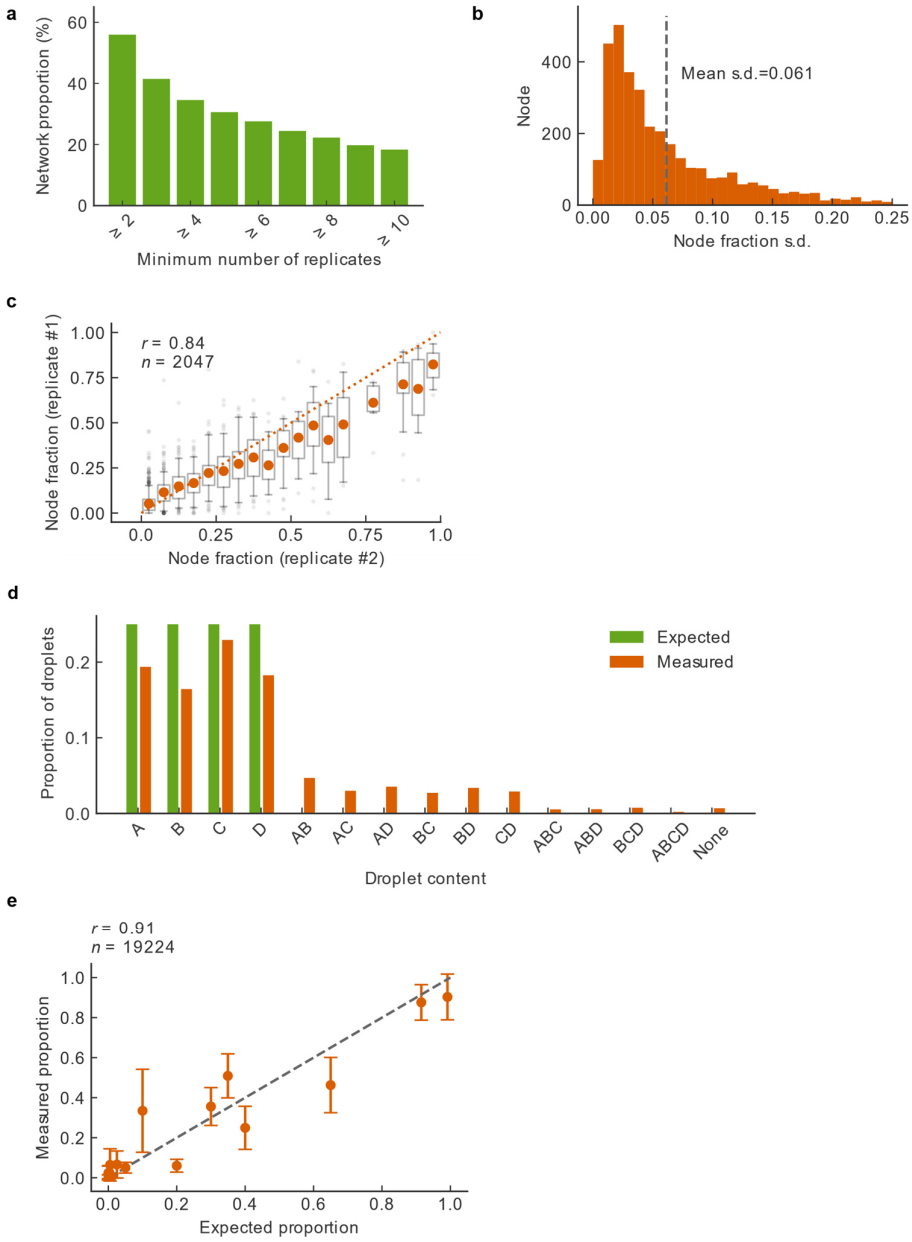

Extended Data Fig. 5. Measurement precision. a, Proportion of unique networks having replicates. 56.0% of the networks in the final dataset have at least duplicates and 18.3% of them have at least 10 replicates. **b**, Distribution of node fraction standard deviation where standard deviation is measured from the networks with at least 5 replicates. The dotted grey line is the mean of the distribution of standard deviation. The result indicates a mean precision of ~6% in species fractions. **c**, The complete experiment (Methods, Extended Data Fig. 1) was replicated and node fractions in both replicates were measured. Node fractions measured in one experimental replicate are plotted against the other. Data is restricted to the common set of networks present in the two replicates. Data points are binned in 20 linearly spaced bins according to their x-axis component. Bins with less than 10 points are discarded. The box extends from the lower to upper quartile values of the data, with a dot at the mean. The whiskers extend from the 5th percentile to the 95th. Flier points are those past the end of the whiskers. The dotted orange line is the identity line. Pearson's correlation coefficient is reported ($p<0.001$, $n=2047$). These technical replicates demonstrated high repeatability ($r=0.84$ between species fractions) **d-e**, Control for cross-talk and quantification bias during droplet barcoding and sequencing. Barcoded sequencing was performed on a mix of four emulsions (A, B, C and D) each containing a mixture of ribozymes in known proportions as well as a pair of

716 specific hairpin RNA reporters for identification (Methods). **d**, Measured proportions of each population of
717 droplets (orange) and expectations (green). The result indicates 87% of sequenced droplet contained a single set
718 of ribozymes which demonstrate a low cross-talk between droplets. **e**, Measured against expected ribozymes
719 concentrations (normalized) aggregating data from the four emulsions show high correlation ($r = 0.91$) and rule
720 out biases of the droplet level sequencing. Each dot corresponds to a ribozyme in one of the emulsions (4 ribozymes
721 in each of the 4 emulsions). Error bars are standard deviations. Grey dotted line is the identity line. Pearson
722 correlation coefficient $p<0.001$ in all cases.

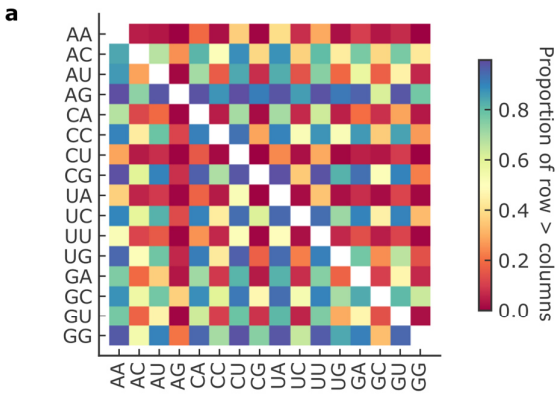

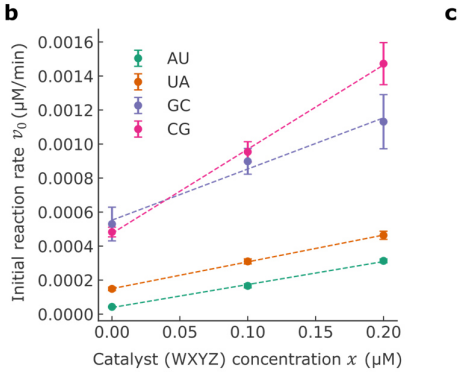

c

$$v_0 = \alpha x + \beta$$

Interaction $M \rightarrow N$	α (min^{-1})	β (μM.min^{-1})	r^2
$A \rightarrow U$	0.001352 ± 0.000041	0.000038 ± 0.000004	0.9975
$U \rightarrow A$	0.001575 ± 0.000097	0.000150 ± 0.000005	0.9998
$C \rightarrow G$	0.004950 ± 0.000283	0.000474 ± 0.000006	0.9993
$G \rightarrow C$	0.003008 ± 0.000335	0.000552 ± 0.000051	0.9833
$G \rightarrow U$	0.000160 ± 0.000007	0.000015 ± 0.000000	0.9997
$U \rightarrow G$	0.000066 ± 0.000001	0.000004 ± 0.000000	0.9986
$A \rightarrow G$	0.000018 ± 0.000000	0.000000 ± 0.000000	0.9279

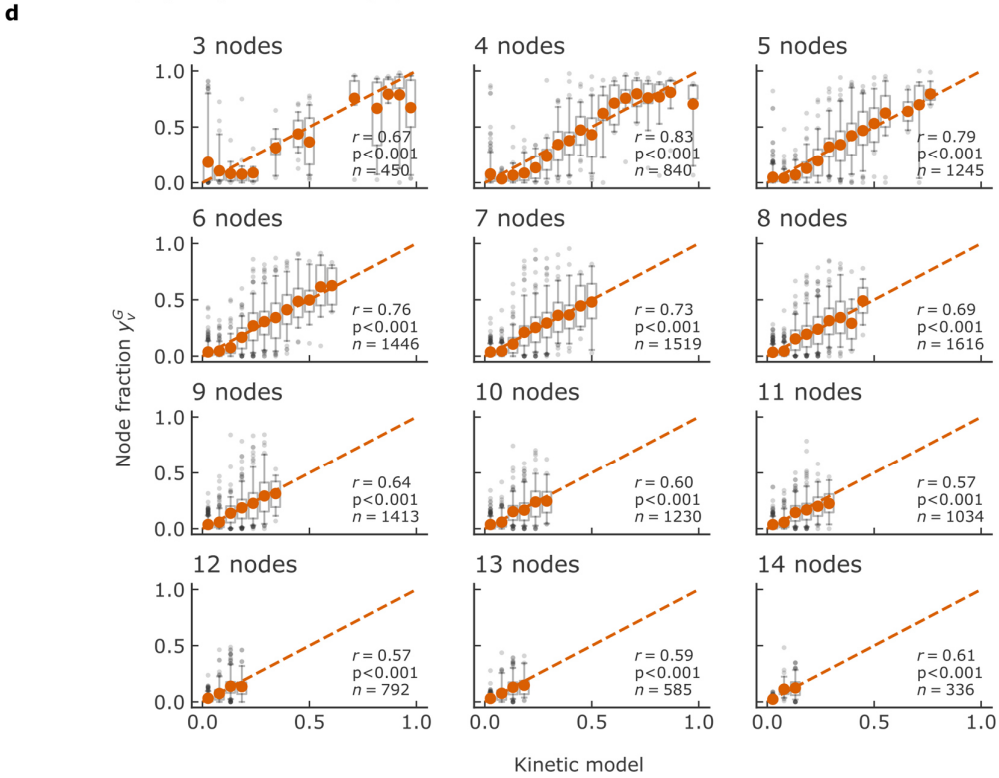

Extended Data Figure 6. Fitting of edge weights in *Azoarcus* networks across various models of node centrality and comparison of the best model with experimental measurements. a, For each pair of nodes, fractions are extracted in all networks that contain the two nodes. The color code indicates the proportion of cases where one node (row) has higher fraction compared to the other node (column). **b-c**, Experimental measurements to extract catalytic parameters used to describe the *Azoarcus* network system[21,35] (Methods). **b**, Plot showing

reaction kinetics for all four Watson-Crick IGS/tag interactions. Initial rates (v_0) of WXYZ formation from WXY and Z RNA fragments were measured by doping the reaction with covalent WXYZ ribozyme with the same IGS and tag as the WXY fragment, as reported by Yeates *et al.*[21]. **c**, Table showing the α and β parameters derived from fitting a linear relationship (top) between the initial rate of formation of WXYZ ribozymes (v_0) as a function of doped covalent WXYZ ribozyme concentration (x)[21,35]. Here α quantifies the synthesis of WXYZ ribozymes catalyzed by covalent ribozymes and, is derived from the slope of this relationship (plot in **b**). Whereas, β quantifies the synthesis of WXYZ ribozymes by non-covalent ribozymes and is derived from the intercept of this relationship (plot in **b**). **d**, Fraction obtained with the kinetic model versus measured fraction for networks with same number of nodes. Bins with less than 10 points are discarded. Dark grey dots are averages; quartile boxplots have 5th - 95th percentiles whiskers with flier points. The dotted orange line is the identity line.

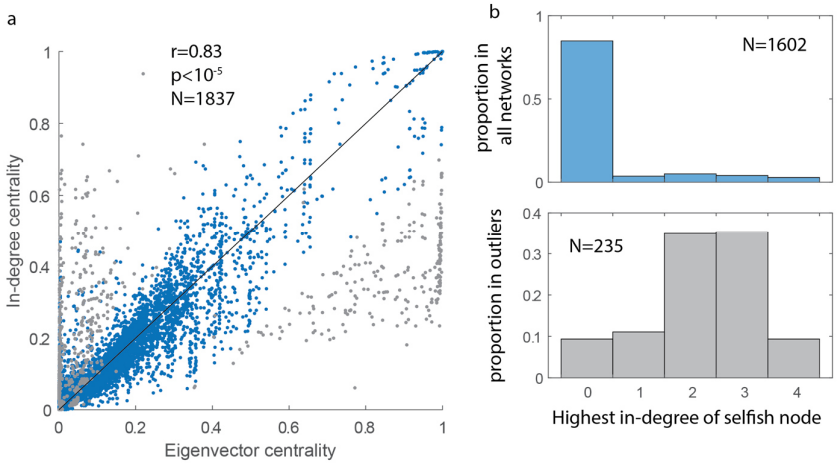

Extended Data Fig. 7. Network composition predictions using eigenvector centrality and in-degree centrality a, Covalent ribozyme fraction predicted by eigenvector centrality versus in-degree centrality for all networks of the experimental dataset (N=1837). In grey are species participating to networks containing outlier ribozymes. The latter are ribozyme species which fraction is underestimated by more than 20% by the in-degree centrality compared to the eigenvector centrality. **b**, Networks containing outliers tend to have selfish nodes (bottom) compared to others (top). Selfishness is quantified here as the in-degree of nodes with self-loops and no out-going edges.

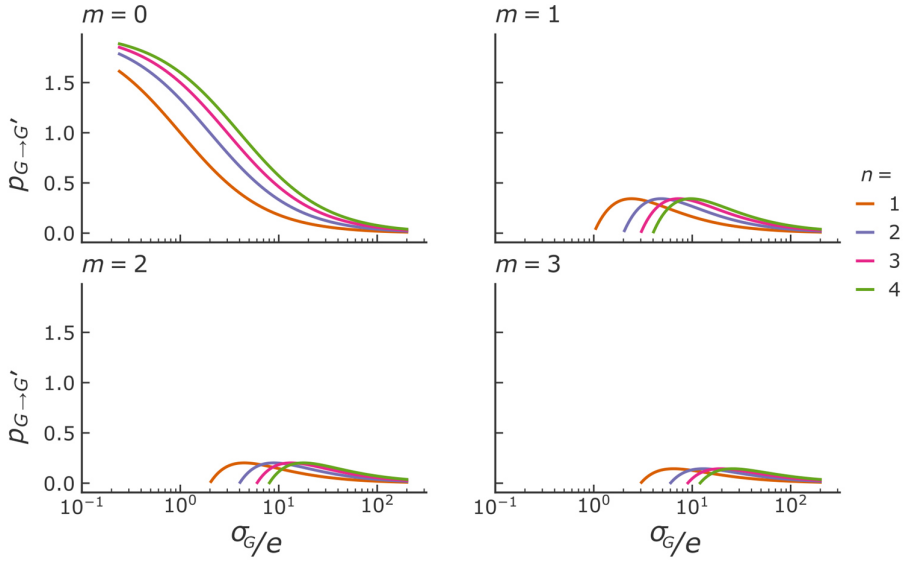

Extended Data Fig. 8. Analytical predictions of Equation 1 with all possible values of the parameters n and m. Network perturbation $p_{G\to G'}$ upon addition of a new node is plotted against normalized background strength σ_G/e for all possible values of the catalytic novelty m (panels) and of perturbation breadth n (color coded).

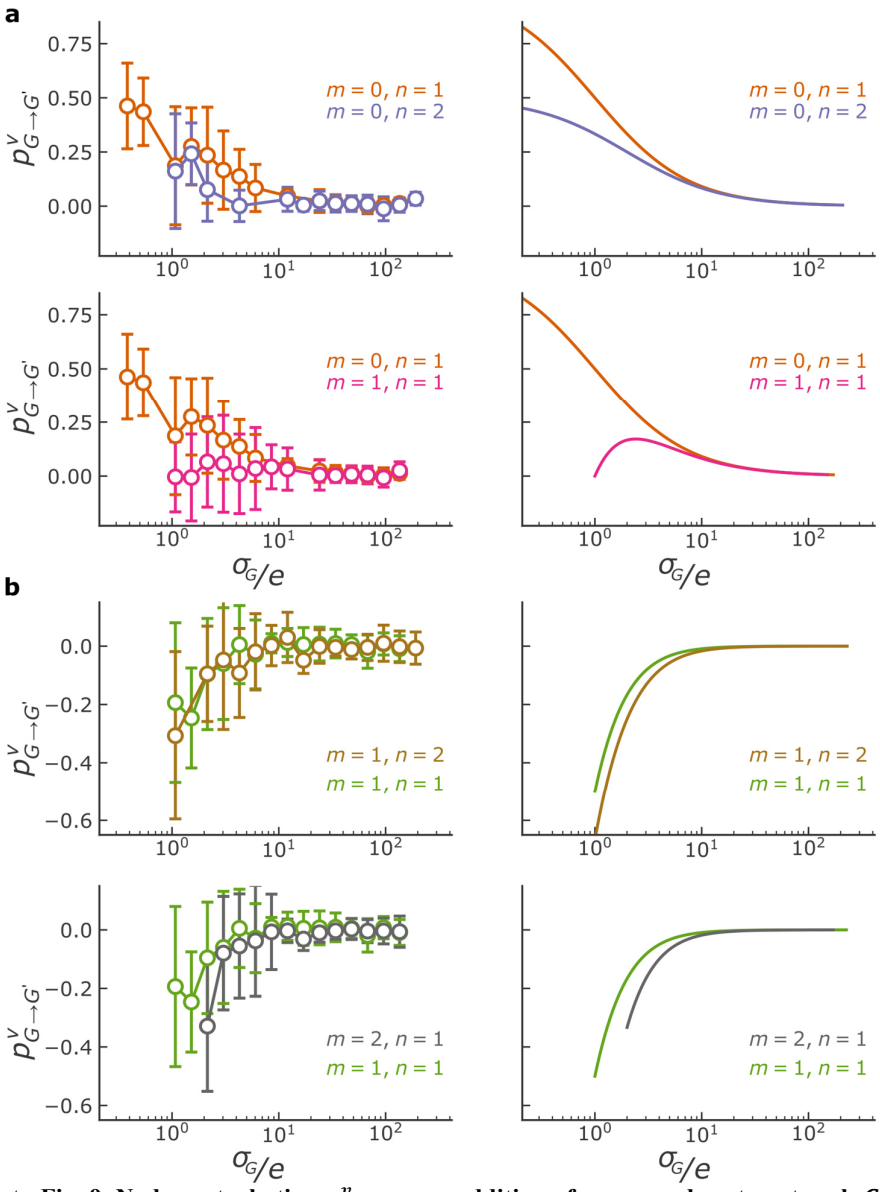

754
755 **Extended Data Fig. 9. Node perturbation $p^v_{G\to G'}$ upon addition of a new node a to network G, comparing**
756 **experimental data with analytical predictions. a**, $p^v_{G\to G'}$ plotted against normalized background strength σ_G/e
757 for different values of catalytic novelty m and perturbation breadth n in the case where v is a target for a and for
758 both the experimental data (left) and the analytical results (right). For details of how analytical predictions were
759 derived see Supplementary File 1. Data points were distributed along the x-axis in 20 log-spaced bins between
760 $10^{-0.5}$ and $10^{2.5}$. Bins with less than 3 points were discarded and the mean and standard deviation for each bin are
761 plotted. Networks with less than 3 nodes were discarded for the analysis. **b**, Same as **a** but the case where v is a
762 not target for a.

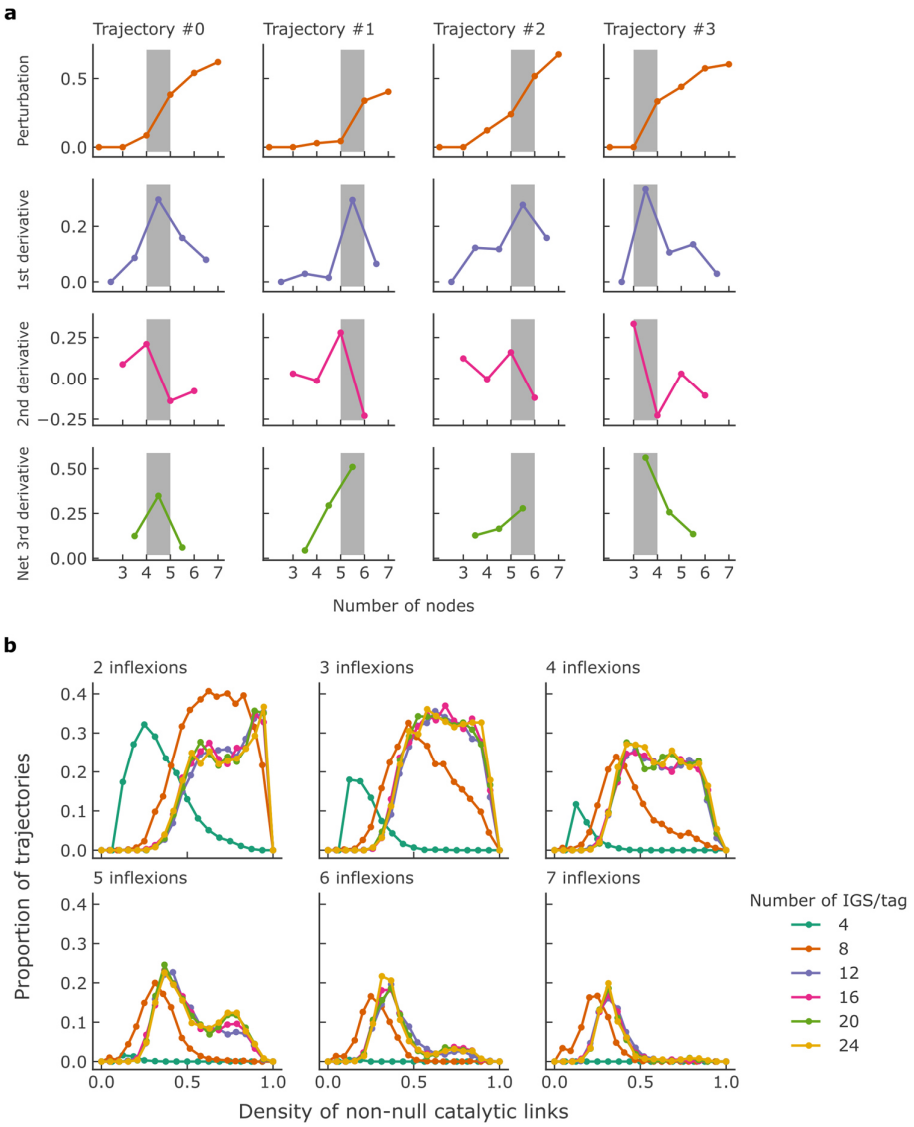

Extended Data Fig. 10. Determination of strong inflexion points and influence of the number of different IGS/tag interactions on the number of inflexion points per trajectory. a, Cumulative perturbation for four representative trajectories from the experimental data are plotted (first row) as well as the first derivative (second row), the second derivative (third row) and the net third derivative (fourth row). The derivative is the difference between two successive points divided by the width of the interval (here 1). Inflexion points are first detected with the second derivative when it switches from positive to negative and the sharpness of these is measured with the net third derivative. Derivatives were computed as the difference of values between n and n+1 nodes. Strong inflexion points are defined as being in the top 25% in sharpness and are indicated with dark grey rectangles. An extra-step with no perturbation is added at the beginning of the trajectory to detect starting strong inflexion points. **b**, Proportion of trajectories with a given number of inflexions plotted against catalytic density for different numbers of IGS/tag combinations. Note that panels corresponding to 6 and 7 inflexions show no trajectory with inflexions when the number of IGS/tag pairs equals 4. Hence analysis of trends holds only when the number of IGS/tag pairs exceeds the number of inflexions, as mentioned in the main text. These results were obtained by simulating 20,000 trajectories as a function of catalytic density values (defined as the proportion of the non-null specific interaction between an IGS and a tag over the complete set of possible interactions) for various number of IGS/tag. See Fig. 4g for the details.

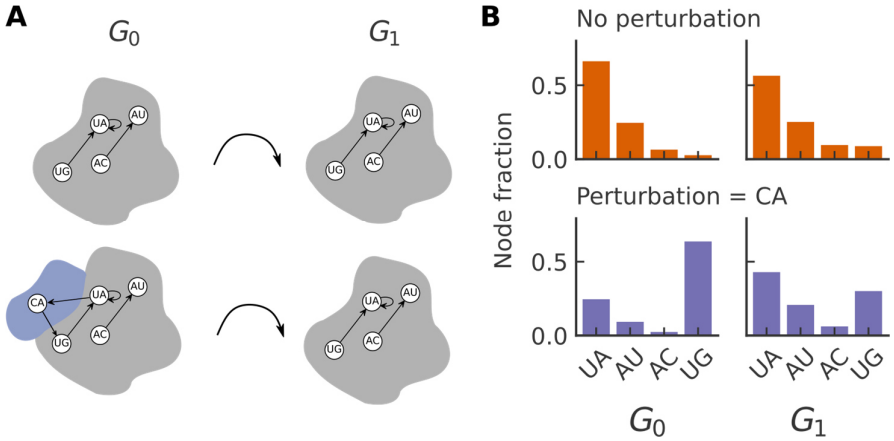

Extended Data Figure 11. Relaxation of chemical compositions to states due to non-covalent catalysts. a, Schematic of two serial transfer experiments with different initial conditions and two generations, G_0 and G_1, incubated for an hour at 48°C as in the droplet experiment. Top: control experiment (unperturbed network), where only the fragment for the AC, AU, UA and UG ribozymes are provided at each round, with concentrations 0.1 μM for WXY fragments and 1.6 μM for Z. Bottom: same as top, but the network is perturbed at G_0 by addition of CA fragments at the same concentration. **b**, Relative fraction of covalent ribozymes AC, AU, UA and UG produced during each generation of the serial transfer. Although introduction of fragments at G_0 has a significant impact on the final covalent ribozyme composition, these differences are not preserved at G_1 where the composition relaxes toward the one of the unperturbed network.

795 **Extended Data Table 1. Different combination of WXY fragments in initial 5 pL emulsions.**

Combination no.	$_{gMg}WXY_{cNu}$ fragments (MN)[#]	Hairpin RNA reporter variable region[¶]
1	UA	UUUU
2	CA	ACUG
3	GA	AAUU
4	AG	GAUA
5	CU	GUGG
6	GC	UAUG
7	UU	CCCA
8	CU, UG	AAGG
9	AC	GGAA
10	CA, GA, CG, UA, AU	AUAG
11	GG, GC	UAAC
12	AU	UGUA
13	CA, UC, GA, CC	UACA
14	AC, AG	CGUG
15	UA, GU, GG, CG, UG, AG, UU, UC	GCCG
16	GG	GAAU
17	AU, CA, AA, AG	GGGU
18	GC	CGCC
19	GU	UUGG
20	CC, GU, CA	GUCC
21	GG, GU, CC	UAGC
22	UU, CU	AAAA
23	CU, CA	CUAA
24	UC	AUGC

796 [#]All 16 possible $_{gMg}WXY_{cNu}$ RNA fragments were used where 'M' is the middle nucleotide of IGS and 'N' is the
797 middle nucleotide of tag[18]. ¶4 nucleotide variable region of the hairpin RNA reporter added to barcode the
798 composition.
799

800 **Extended Data Table 2. Variation in growth for different sizes of networks.**

Number of nodes	Number of networks	Mean yield (nM)	SD yield (nM)	Minimum growth (nM)	Maximum growth (nM)	Fold difference max/min growth
2	22	37.3	19.1	10.4	95.1	9.1
3	48	49.6	29.5	19.3	151.2	7.8
4	60	56.0	26.4	25.6	146.9	5.8
5	47	84.0	37.5	26.4	162.1	6.1
6	47	113.9	43.8	52.4	233.3	4.5
7	27	142.7	38.6	91.9	222.6	2.4
8	17	181.7	67.9	92.6	373.1	4.0
9	9	280.6	45.4	184.4	328.3	1.8
10	16	303.4	60.3	203.4	405.5	2.0
11	10	371.9	86.9	236.8	481.3	2.0
12	15	371.3	95.7	240.8	654.6	2.7
13	10	367.8	70.7	260.2	452.6	1.7
14	5	419.1	36.2	381.0	459.5	1.2
15	3	394.9	40.7	359.8	439.5	1.2

801